

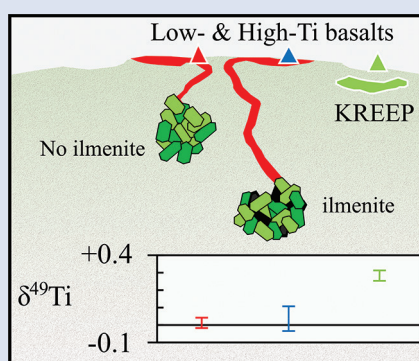
Unravelling lunar mantle source processes via the Ti isotope composition of lunar basalts

S. Kommescher^{1*}, R.O.C. Fonseca^{1,2}, F. Kurzweil¹,
M.M. Thiemens^{1,3}, C. Münker^{1,4}, P. Sprung^{1,4}

OPEN ACCESS

doi: 10.7185/geochemlet.2007

Abstract



Formation and crystallisation of the Lunar Magma Ocean (LMO) was one of the most incisive events during the early evolution of the Moon. Lunar Magma Ocean solidification concluded with the coeval formation of K-, REE- and P-rich components (KREEP) and an ilmenite-bearing cumulate (IBC) layer. Gravitational overturn of the lunar mantle generated eruptions of basaltic rocks with variable Ti contents, of which their $\delta^{49}\text{Ti}$ variations may now reflect variable mixtures of ambient lunar mantle and the IBC. To better understand the processes generating the spectrum of lunar low-Ti and high-Ti basalts and the role of Ti-rich phases such as ilmenite, we determined the mass dependent Ti isotope composition of four KREEP-rich samples, 12 low-Ti, and eight high-Ti mare basalts by using a ^{47}Ti - ^{49}Ti double spike. Our data reveal significant variations in $\delta^{49}\text{Ti}$ for KREEP-rich samples (+0.117 to +0.296 ‰) and intra-group variations in the mare basalts (-0.030 to +0.055 ‰ for low-Ti and +0.009 to +0.115 ‰ for high-Ti basalts). We modelled the $\delta^{49}\text{Ti}$ of KREEP using previously published HFSE data as well as

the $\delta^{49}\text{Ti}$ evolution during fractional crystallisation of the LMO. Both approaches yield $\delta^{49}\text{Ti}_{\text{KREEP}}$ similar to measured values and are in excellent agreement with previous studies. The involvement of ilmenite in the petrogenesis of the lunar mare basalts is further evaluated by combining our results with element ratios of HFSE, U and Th, revealing that partial melting in an overturned lunar mantle and fractional crystallisation of ilmenite must be the main processes accounting for mass dependent Ti isotope variations in lunar basalts. Based on our results we can also exclude formation of high-Ti basalts by simple assimilation of ilmenite by ascending melts from the depleted lunar mantle. Rather, our data are in accord with melting of these basalts from a hybrid mantle source formed in the aftermath of gravitational lunar mantle overturn, which is in good agreement with previous Fe isotope data.

Received 5 August 2019 | Accepted 24 January 2020 | Published 28 February 2020

Introduction

It is widely accepted that the Moon formed as the result of an impact between one or more planetesimals and the proto-Earth (e.g., Asphaug, 2014). The last phases to solidify in the impact-induced Lunar Magma Ocean (LMO) were K-, REE-, and P-rich residual components (urKREEP) and complementarily an ilmenite-bearing cumulate (IBC; Warren and Wasson, 1979; Snyder *et al.*, 1992). Subsequent magmatic processes concluded with the eruption of lunar mare basalts (e.g., Gross and Joy, 2016). Experimental studies and the Hf and Nd isotope composition of mare basalts suggest that low-Ti mare basalts likely result from partial melting of lunar mafic cumulates, whereas high-Ti mare basalts are thought to reflect IBC involvement (e.g., Longhi, 1992; Sprung *et al.*, 2013). However, whether high-Ti basalts result from IBC assimilation by mafic low-Ti magmas (e.g., Münker, 2010), or from the partial melting of a

hybridised lunar mantle source (Snyder *et al.*, 1992), remains ambiguous. Titanium isotope variations in mare basalts may be used to discriminate between the two scenarios: refractory, lithophile, and fluid-immobile Ti is predominantly tetravalent albeit lunar samples may contain significant amounts of Ti^{3+} (Simon and Sutton, 2017; Leitzke *et al.*, 2018). The principal Ti-bearing phase in the lunar mantle is ilmenite whose VI fold coordinated crystal site preferentially incorporates lighter over heavier Ti isotopes (Schauble, 2004). The Ti isotope composition of terrestrial samples (given as $\delta^{(49}\text{Ti}/^{47}\text{Ti})_{\text{OL-Ti}}$, relative to the Origins Lab reference material, henceforth $\delta^{49}\text{Ti}$; Millet and Dauphas, 2014) ranges between -0.046 and +1.8 ‰. Observed covariations between $\delta^{49}\text{Ti}$ and SiO_2 , TiO_2 , and FeO contents of terrestrial volcanic rocks suggest that stable Ti isotope variation is mainly driven by the onset of fractional crystallisation of Fe-Ti oxides during magmatic differentiation (Millet *et al.*, 2016; Greber *et al.*, 2017a,b; Deng *et al.*, 2018a, 2019; Mandl

1. Institut für Geologie und Mineralogie, Universität zu Köln, Germany
 2. Institut für Geologie, Mineralogie und Geophysik, Ruhr-Universität Bochum, Germany
 3. G-TIME Laboratory, Université Libre de Bruxelles, Belgium
 4. Hot Laboratory Division (AHL), Paul Scherer Institut, Villigen, Switzerland
- * Corresponding author (e-mail: s.kommescher@uni-koeln.de)



et al., 2018). Consequently, the Ti isotope composition of lunar magmas might be a sensitive indicator for the crystallisation of the IBC, and its assimilation or partial melting: Millet *et al.* (2016) reported $\delta^{49}\text{Ti}$ variations in three low-Ti mare basalts with a pooled $\delta^{49}\text{Ti}$ of -0.008 ± 0.019 ‰ and five high-Ti mare basalts with $\delta^{49}\text{Ti}$ between $+0.011$ and $+0.033$ ‰. The presence of more fractionated $\delta^{49}\text{Ti}$ in mare basalts, although suggested, has not yet been reported (Millet *et al.*, 2016). Indeed, for the urKREEP end member, as represented by the lunar meteorite Sayh al Uhaymir (SaU) 169, a tentative $\delta^{49}\text{Ti}$ of $+0.330 \pm 0.034$ ‰ was obtained (Greber *et al.*, 2017b).

Here we report the $\delta^{49}\text{Ti}$ of 24 representative lunar samples in order to investigate their mantle sources in the context of three major end members: the ambient lunar mantle (low-Ti), the late stage cumulates (IBC, high-Ti), and the residual KREEP-rich component. Notably, the processes that affect $\delta^{49}\text{Ti}$ in lunar mantle cumulates and corresponding melts also fractionate high field strength element ratios (HFSE; Münker, 2010). High precision HFSE, W, U, and Th data, obtained for the same samples (Thiemens *et al.*, 2019), can help to constrain $\delta^{49}\text{Ti}_{\text{urKREEP}}$, $\delta^{49}\text{Ti}_{\text{IBC}}$ and to identify the processes leading to $\delta^{49}\text{Ti}$ variations in lunar samples.

Results

Titanium isotope measurements were performed using the Thermo Neptune Plus MC-ICPMS at the University of Cologne with an intermediate precision better than ± 0.023 ‰ (2 × standard deviation, henceforth s.d.) for spiked reference materials BCR-2, JB-2, OL-Ti, and Col-Ti. Total blank contribution was always less than 10 ng total Ti and is negligible compared to at least 30 µg of processed sample Ti (20 µg for 68115). More detailed information on the analytical protocol are given in the Supplementary Information. Low-Ti mare basalts show small, resolvable variations in $\delta^{49}\text{Ti}$ between -0.030 and $+0.055$ ‰ with an average of $+0.010 \pm 0.015$ ‰ (2 s.d.; $n = 12$, Fig. 1, Table 1). Most high-Ti samples range from $+0.009$ to $+0.047$ in $\delta^{49}\text{Ti}$ (average of $+0.026 \pm 0.036$ ‰, 2 s.d.; $n = 7$), sample 75035 has a comparatively high $\delta^{49}\text{Ti}$ value of $+0.115$ ‰. The high-Ti average (including 75035) yields a $\delta^{49}\text{Ti}$ of $+0.037 \pm 0.071$ ‰. KREEP-rich lithologies have $\delta^{49}\text{Ti}$ values between $+0.117$ and $+0.296$ ‰.

Discussion

Estimating the $\delta^{49}\text{Ti}$ of urKREEP and the IBC. The co-genetic relationship between urKREEP and IBC permits studying the coupled $\delta^{49}\text{Ti}$ evolution of both reservoirs. Complementary to the low $\delta^{49}\text{Ti}_{\text{IBC}}$, the residual LMO is expected to have positive $\delta^{49}\text{Ti}$ (Millet *et al.*, 2016; Greber *et al.*, 2017b). Furthermore, U became enriched in urKREEP, whereas Ti, Hf and Zr are more compatible in ilmenite and are extracted from the LMO during IBC formation. The observed positive co-variation of $\delta^{49}\text{Ti}$ and U concentration in KREEP-rich samples may therefore indicate variable portions of the urKREEP-component (Fig. 2b). Our KREEP-rich sample with highest $\delta^{49}\text{Ti}$ and highest U concentration is identical within uncertainty to the previous estimate for $\delta^{49}\text{Ti}_{\text{urKREEP}}$ (Greber *et al.*, 2017b). Two KREEP-rich samples along with SaU169 have U/Hf, U/Zr and U/Ti in the range of the urKREEP estimate (calculated using data by Warren and Taylor, 2014), which results in a conservative estimate of $\delta^{49}\text{Ti}_{\text{urKREEP}}$ of $+0.296 \pm 0.067$ ‰ (see Supplementary Information). To model $\delta^{49}\text{Ti}_{\text{urKREEP}}$ in a different approach, we constrained the evolution of Ti, Hf and Ta concentrations in the remaining liquid during fractional crystallisation for various LMO solidification models (Snyder *et al.*, 1992; Lin *et al.*, 2017; Charlier *et al.*, 2018; Rapp

Table 1 Summary of reference materials and measured samples. For reference materials, n gives the number of sequences in which the material has been measured at least 6 times. Abbreviations are the same as in Figure 1. Two aliquots of OL-Ti were run through the chemical separation process and are given as OL-Ti (chemistry).

			$\delta^{49}\text{Ti}$	2 s.d.	n	95 % c.i.
JB-2			-0.044	0.023	7	0.011
BCR-2			-0.025	0.012	4	0.010
OL-Ti mean			0.000	0.001	8	0.000
OL-Ti (chemistry)			-0.001	0.030	2	0.137
Col-Ti mean			0.206	0.021	8	0.009
<i>Low-Ti rocks</i>						
12022	Apollo 12	Low-Ti ilm basalt	0.029	0.022	6	0.011
12051	"	Low-Ti ilm basalt	0.030	0.022	8	0.009
12063	"	Low-Ti ilm basalt	0.055	0.022	6	0.012
12054	"	Low-Ti ilm basalt	0.028	0.026	6	0.014
12004	"	Low-Ti olv basalt	0.006	0.010	6	0.005
12053	"	Low-Ti pgt basalt	-0.013	0.026	6	0.014
15495	Apollo 15	Low-Ti ONB	0.011	0.017	6	0.009
15555	"	Low-Ti ONB	-0.008	0.026	6	0.014
15556	"	Low-Ti ONB	0.007	0.030	6	0.016
15065	"	Low-Ti QNB	-0.030	0.014	6	0.007
15058	"	Low-Ti QNB	-0.010	0.034	6	0.018
15545	"	Low-Ti QNB	0.011	0.032	6	0.017
Low-Ti mean \pm 2 s.d.			0.010	0.047	12	
<i>High-Ti rocks</i>						
10017	Apollo 11	High-Ti ilm basalt	0.009	0.024	6	0.012
10020	"	High-Ti ilm basalt	0.011	0.022	6	0.011
10057	"	High-Ti ilm basalt	0.009	0.024	6	0.012
74255	Apollo 17	High-Ti ilm basalt	0.043	0.010	6	0.005
74275	"	High-Ti ilm basalt	0.045	0.010	6	0.005
75035	"	High-Ti ilm basalt	0.115	0.025	6	0.013
79135	"	High-Ti bce	0.019	0.017	6	0.009
79035	"	High-Ti bce	0.047	0.018	6	0.010
High-Ti mean 1 \pm 2 s.d.			0.026	0.036	7	
High-Ti mean 2 \pm 2 s.d.			0.037	0.071	8	
<i>KREEP-rich rocks</i>						
14305	Apollo 14	KREEP-rich bce	0.296	0.030	6	0.016
14310	"	KREEP basalt	0.263	0.035	6	0.018
72275	Apollo 17	KREEP-rich bce	0.185	0.026	6	0.014
68115	Apollo 16	KREEP-rich bce	0.117	0.027	6	0.014

and Draper, 2018) starting with LMO element abundances by Münker (2010) and calculated $\delta^{49}\text{Ti}_{\text{melt}}$ using a Rayleigh distillation model (see Supplementary Information). The intersect of the respective Ti, Hf and Ta concentrations with urKREEP concentration estimates by Warren and Taylor (2014) together with the modelled $\delta^{49}\text{Ti}_{\text{melt}}$ -evolution line yield a range for $\delta^{49}\text{Ti}_{\text{urKREEP}}$: all estimates using the above mentioned models and LMO concentrations of Ta ($\delta^{49}\text{Ti}_{\text{urKREEP}} = +0.308 \pm 0.064$ ‰), Hf ($\delta^{49}\text{Ti}_{\text{urKREEP}} = +0.290 \pm 0.040$ ‰) and Ti ($\delta^{49}\text{Ti}_{\text{urKREEP}} = +0.238 \pm 0.085$ ‰) are identical to our KREEP-rich sample with highest $\delta^{49}\text{Ti}$ ($+0.296 \pm 0.016$ ‰), and previous estimates for $\delta^{49}\text{Ti}_{\text{urKREEP}}$ (Greber *et al.*, 2017b). Our models predict a final $\delta^{49}\text{Ti}_{\text{IBC}}$ between -0.006 and -0.012 ‰, consistent with estimates by Millet *et al.* (2016).



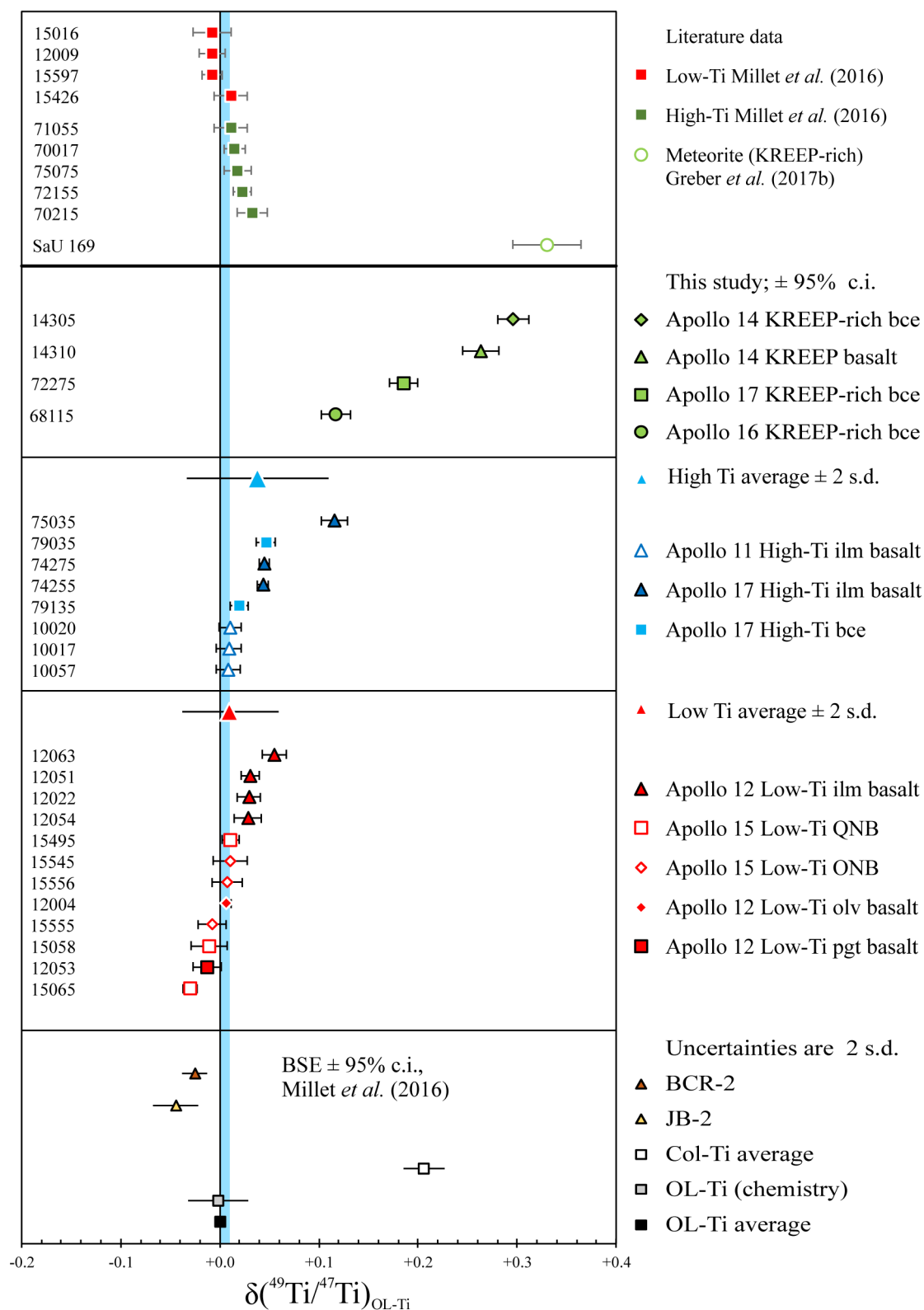


Figure 1 Measured Ti isotope compositions of lunar samples. All uncertainties unless stated otherwise are 95 % confidence interval (c.i.) of at least 6 measurements of the same aliquot. See main text and Supplementary Information for details. bce = breccia, ilm = ilmenite; QNB = quartz-normative basalt, olv = olivine, pgt = pigeonite.

Identifying magmatic processes in lunar basalt sources. The average $\delta^{49}\text{Ti}$ values obtained for low- and high-Ti mare basalts ($+0.010 \pm 0.047$ ‰ and $+0.037 \pm 0.071$ ‰) are consistent with findings by Millet *et al.* (2016) and are indistinguishable from their Bulk Silicate Earth estimate (BSE: $+0.005 \pm 0.005$ ‰, 95 % c.i.; see Fig. 1). The $\delta^{49}\text{Ti}$ value of our most primitive sample, the Apollo 12 olivine basalt

12004 (possibly tapping bulk lunar mantle) is identical with the $\delta^{49}\text{Ti}_{\text{BSE}}$ estimate by Millet *et al.* (2016) and the chondritic $\delta^{49}\text{Ti}$ value proposed by Greber *et al.* (2017b) but lower than the chondritic $\delta^{49}\text{Ti}$ value suggested by Deng *et al.* (2018b). Possible explanations for the observed intra-group $\delta^{49}\text{Ti}$ variations in mare basalts include fractional crystallisation of ilmenite during petrogenesis, assimilation of an IBC- or



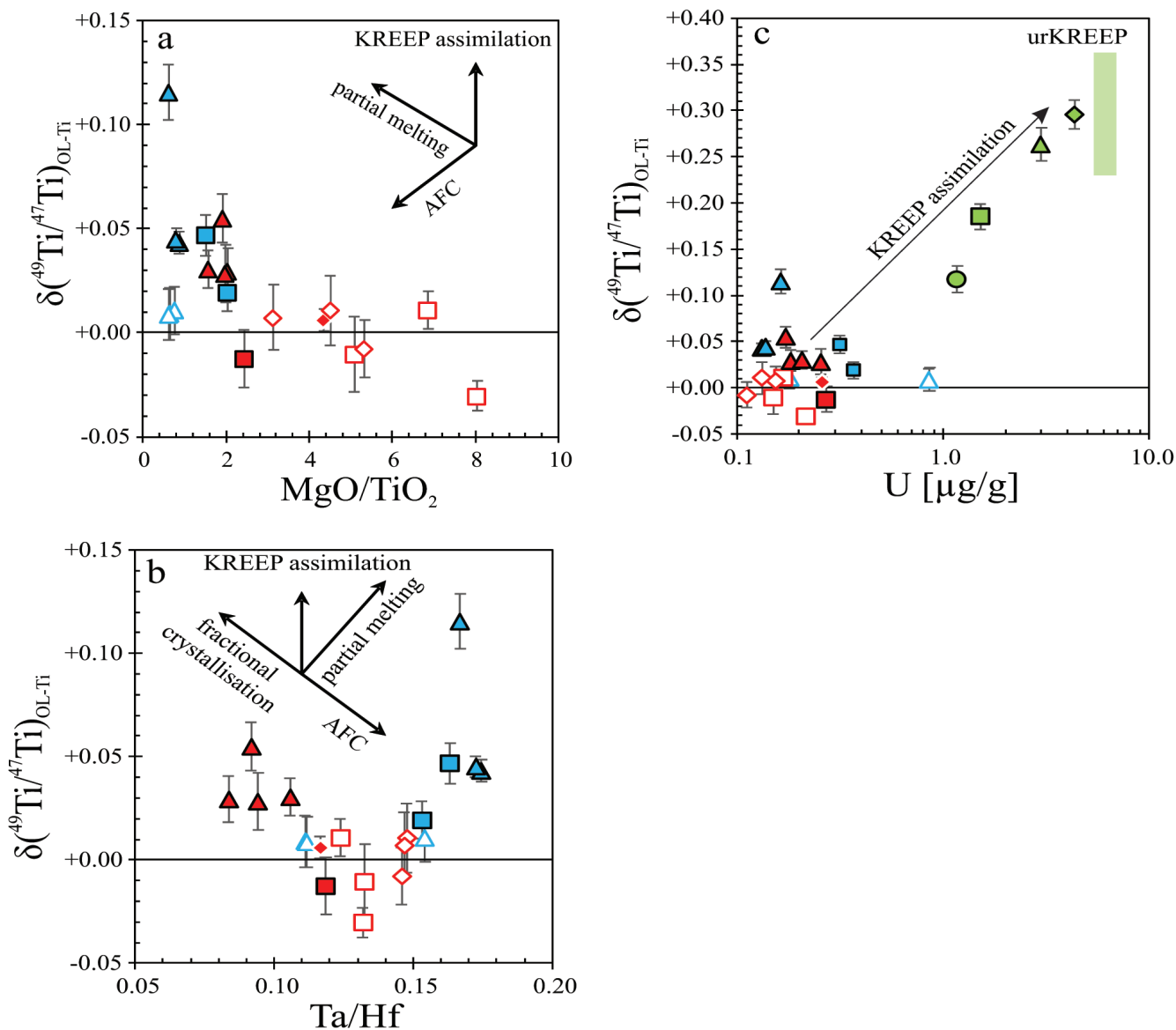


Figure 2 Plots of (a) $\delta^{49}\text{Ti}$ vs. MgO/TiO_2 , (b) $\delta^{49}\text{Ti}$ vs. Ta/Hf and (c) $\delta^{49}\text{Ti}$ vs. U that can be used to discriminate between processes leading to variations in $\delta^{49}\text{Ti}$. Symbols are the same as in Figure 1, black arrows indicate the direction in which a process would influence the values along y- and x-axes. Partial melting assumes the presence of ilmenite in the source, fractional crystallisation always implies fractional crystallisation of ilmenite. AFC implies the assimilation of an IBC component during ilmenite-free fractional crystallisation of a low-Ti magma. (b) The estimated Ta/Hf value of urKREEP is ~ 0.11 (Warren and Taylor, 2014). (c) Contamination by urKREEP (coloured arrow), would imply higher U contents (not observed). urKREEP is based on our first model (see Supplementary Information).

KREEP-component during fractional crystallisation, partial melting an IBC or mantle source heterogeneity. To distinguish between these processes we first consider the results of experimental studies that simulated the petrogenesis of lunar basalts (see Supplementary Information; Longhi, 1992 and references therein): For instance, experimentally synthesised low-Ti-like samples showed that ilmenite has been one of the first solidus phases (Longhi, 1992 and references therein), which would preferentially incorporate light Ti isotopes, increasing the $\delta^{49}\text{Ti}_{\text{melt}}$ during fractional crystallisation of ilmenite (Millet *et al.*, 2016). High-Ti basalts from Apollo 17 were shown to originate from greater depths than Apollo 12 and 15 low-Ti mare basalts were successfully modelled by partial melting of an ilmenite-rich source (Longhi, 1992 and references therein). This can explain the observed elevated $\delta^{49}\text{Ti}_{\text{high-Ti}}$ values (See Fig. 2a; Millet *et al.*, 2016). In contrast, the full assimilation of an IBC-component during fractional crystallisation of a low-Ti magma would decrease the $\delta^{49}\text{Ti}$ value of the basaltic melt (Fig. 2a). Thus, the small intra-group variations in $\delta^{49}\text{Ti}$ values

of low- and high-Ti basalts can best be explained by fractional crystallisation of ilmenite and melting of ilmenite-bearing sources, respectively.

In addition to experimental petrological studies, geochemical tools can help distinguish between the discussed processes. For example, the compatibility of HFSEs in ilmenite is variable (Münker, 2010): tantalum is the most compatible HFSE in ilmenite, whereas Hf is the most incompatible (*e.g.*, $D_{\text{Ta}} > 1 > D_{\text{Hf}}$; Leitzke *et al.*, 2016; or $D_{\text{Ta}} > D_{\text{Hf}}$, van Kan Parker *et al.*, 2011). Thus, fractional crystallisation of ilmenite would increase the $\delta^{49}\text{Ti}_{\text{melt}}$ (Millet *et al.*, 2016) but decrease the $\text{Ta}/\text{Hf}_{\text{melt}}$ (Münker, 2010). In contrast, partial melting of an IBC component would increase the $\text{Ta}/\text{Hf}_{\text{melt}}$ and the $\delta^{49}\text{Ti}_{\text{melt}}$ value ($D_{\text{Ta}} \sim 2 \times D_{\text{Hf}}$ for ilmenite, *e.g.*, Leitzke *et al.*, 2016). Apollo 12 low-Ti ilmenite basalts show lower Ta/Hf and positive $\delta^{49}\text{Ti}$ relative to the most primitive lunar basalt analysed in this study, (12004, see Figs. 1, 2b), indicating the early fractional crystallisation of ilmenite, which is consistent with



experimental results (Longhi, 1992 and references therein). Relatively low $\delta^{49}\text{Ti}$ values in Apollo 15 low-Ti basalts may indicate the assimilation of an IBC material (Longhi, 1992 and references therein). However, assimilation of an IBC component seems inconsistent with relatively low Ta/Hf and comparatively low TiO_2 contents of $\sim 1.3\%$. The assimilation of a KREEP-component would cause a substantial increase in the $\delta^{49}\text{Ti}$ and U concentration of the melt while barely fractionating Ta/Hf. Such trends are not observed indicating that KREEP components played an insignificant role during the petrogenesis of low- and high-Ti basalts (Fig. 2c). Apollo 17 high-Ti samples are rich in TiO_2 , exhibit relatively low MgO/TiO_2 but high $\delta^{49}\text{Ti}$ and higher Ta/Hf relative to our most primitive sample. In agreement with the experimental evidence, this geochemical pattern strongly indicates partial melting of an IBC component during the petrogenesis of Apollo 17 high-Ti basalts (Longhi, 1992 and references therein). These processes are further modelled and discussed in the Supplementary Information.

Comparison with Fe isotope systematics. Previous studies observed a bimodal distribution of $\delta^{57}\text{Fe}$ values for lunar low-Ti and high-Ti basalts: higher $\delta^{57}\text{Fe}$ values in high-Ti basalts were attributed to the presence of ilmenite during partial melting (Sossi and Moynier, 2017; Sossi and O'Neill, 2017), which is consistent with experimental studies (Longhi, 1992 and references therein) as well as our Ta/Hf and $\delta^{49}\text{Ti}$ data. However, intra-group variation in $\delta^{57}\text{Fe}$ of low-Ti basalts was not observed (Weyer *et al.*, 2005; Sossi and Moynier, 2017; Poitrasson *et al.*, 2019) as the $\delta^{57}\text{Fe}$ of low-Ti basalts is mainly controlled by fractional crystallisation of olivine and pyroxene, which would preferentially incorporate light Fe isotopes, similar to ilmenite ($\Delta^{57}\text{Fe}_{\text{Ilm-Ol}} = +0.01\%$; Sossi and O'Neill, 2017). Thus, $\delta^{49}\text{Ti}$ appear more appropriate to discriminate better between the petrogenetic processes culminating in lunar basalts. Additional Cr, V and Hf isotope systematics are discussed in the Supplementary Information.

Conclusion

New Ti isotope data for a representative set of lunar samples show that there is a clear offset between KREEP-rich samples and mare basalts, in agreement with previous work (Millet *et al.*, 2016; Greber *et al.*, 2017b). Our data reveal intra-group variation amongst olivine- and quartz-normative and (low-Ti) ilmenite mare basalts with the latter recording higher $\delta^{49}\text{Ti}$ than the former. High-Ti mare basalts have overall higher $\delta^{49}\text{Ti}$. The $\delta^{49}\text{Ti}$ of our lunar sample suite, coupled with HFSE data, suggests that the fractional crystallisation of ilmenite and partial melting of an IBC-component are the principal processes affecting the $\delta^{49}\text{Ti}$ of Apollo 12 low-Ti mare basalts, and of Apollo 17 high-Ti mare basalts, respectively. This conclusion is consistent with results of previously published experimental studies (Longhi, 1992 and references therein). This is in excellent agreement with previous experimental data and the heavy $\delta^{57}\text{Fe}$ of high-Ti mare basalts (Longhi, 1992; Weyer *et al.*, 2005; Sossi and Moynier, 2017; Charlier *et al.*, 2018). Based on coupled HFSE and $\delta^{49}\text{Ti}$ data, the petrogenesis of high-Ti mare basalts by assimilation of IBC-component by low-Ti magma is unlikely.

Acknowledgements

We thank CAPTEM for providing lunar samples and Horst Marschall for handling the manuscript. The authors would like to thank Marc-Alban Millet and Nicolas Greber for sharing the OL-Ti reference material, Wim van Westrenen and one anonymous reviewer for constructive comments that greatly

improved the manuscript. ROCF is grateful for funding of a Heisenberg Professorship by the Deutsche Forschungsgemeinschaft (DFG grants FO 698/6-1 and FO 698/11-1). CM acknowledges funding by the European Research Council (ERC) under the European Union's Horizon 2020 research and innovation programme (grant agreement No. 669666). SK was partially funded through a UoC Advanced Post Doc grant within the Excellence Initiative to PS and acknowledges the UoC Graduate School of Geosciences for providing a fellowship (GSGS-2019X-07).

Editor: Horst R. Marschall

Additional Information

Supplementary Information accompanies this letter at <http://www.geochemicalperspectivesletters.org/article2007>.



This work is distributed under the Creative Commons Attribution Non-Commercial No-Derivatives 4.0 License, which permits unrestricted distribution provided the original author and source are credited. The material may not be adapted (remixed, transformed or built upon) or used for commercial purposes without written permission from the author. Additional information is available at <http://www.geochemicalperspectivesletters.org/copyright-and-permissions>.

Cite this letter as: Kommescher, S., Fonseca, R.O.C., Kurzweil, F., Thiemens, M.M., Munker, C., Sprung, P. (2020) Unravelling lunar mantle source processes via the Ti isotope composition of lunar basalts. *Geochem. Persp. Let.* 13, 13–18.

References

- ASPHAUG, E. (2014) Impact Origin of the Moon? *Annual Review of Earth and Planetary Sciences* 42, 551–578.
- CHARLIER, B., GROVE, T.L., NAMUR, O., HOLTZ, F. (2018) Crystallization of the lunar magma ocean and the primordial mantle-crust differentiation of the Moon. *Geochimica et Cosmochimica Acta* 234, 50–69.
- DENG, Z., CHAUSSIDON, M., SAVAGE, P., ROBERT, F., PIK, R., MOYNIER, F. (2019) Titanium isotopes as a tracer for the plume or island arc affinity of felsic rocks. *Proceedings of the National Academy of Sciences* 201809164.
- DENG, Z., MOYNIER, F., SOSSI, P.A., CHAUSSIDON, M. (2018a) Bridging the depleted MORB mantle and the continental crust using titanium isotopes. *Geochemical Perspectives Letters* 9, 11–15.
- DENG, Z., MOYNIER, F., VAN ZUILEN, K., SOSSI, P.A., PRINGLE, E.A., CHAUSSIDON, M. (2018b) Lack of resolvable titanium stable isotopic variations in bulk chondrites. *Geochimica et Cosmochimica Acta* 239, 409–419.
- GREBER, N.D., DAUPHAS, N., BEKKER, A., PTÁČEK, M.P., BINDEMAN, I.N., HOFMANN, A. (2017a) Titanium isotopic evidence for felsic crust and plate tectonics 3.5 billion years ago. *Science* 357, 1271–1274.
- GREBER, N.D., DAUPHAS, N., PUCHTEL, I.S., HOFMANN, B.A., ARNDT, N.T. (2017b) Titanium stable isotopic variations in chondrites, achondrites and lunar rocks. *Geochimica et Cosmochimica Acta* 213, 534–552.
- GROSS, J., JOY, K.H. (2016) Evolution, Lunar: From Magma Ocean to Crust Formation. In: Cudnik, B. (Ed.) *Encyclopedia of Lunar Science*. Springer International Publishing, Cham, 1–20.
- LEITZKE, F.P., FONSECA, R.O.C., MICHELY, L.T., SPRUNG, P., MÜNKER, C., HEUSER, A., BLANCHARD, H. (2016) The effect of titanium on the partitioning behavior of high-field strength elements between silicates, oxides and lunar basaltic melts with applications to the origin of mare basalts. *Chemical Geology* 440, 219–238.
- LEITZKE, F.P., FONSECA, R.O.C., GÖTTLICHER, J., STEININGER, R., JAHN, S., PRESCHER, C., LAGOS, M. (2018) Ti K-edge XANES study on the coordination number and oxidation state of Titanium in pyroxene, olivine, armalcolite, ilmenite, and silicate glass during mare basalt petrogenesis. *Contributions to Mineralogy and Petrology* 173, 103.



- LIN, Y., TRONCHE, E.J., STEENSTRA, E.S., VAN WESTRENNEN, W. (2017) Experimental constraints on the solidification of a nominally dry lunar magma ocean. *Earth and Planetary Science Letters* 471, 104–116.
- LONGHI, J. (1992) Experimental petrology and petrogenesis of mare volcanics. *Geochimica et Cosmochimica Acta* 56, 2235–2251.
- MANDL, M.B., FEHR, M.A., SCHÖNBÄCHLER, M. (2018) Titanium stable isotope fractionation on the Moon: Evidence for inter-mineral isotopic fractionation. *Goldschmidt Abstracts* 2018 1666.
- MILLET, M.-A., DAUPHAS, N. (2014) Ultra-precise titanium stable isotope measurements by double-spike high resolution MC-ICP-MS. *Journal of Analytical Atomic Spectrometry* 29, 1444.
- MILLET, M.-A., DAUPHAS, N., GREBER, N.D., BURTON, K.W., DALE, C.W., DEBRET, B., MACPHERSON, C.G., NOWELL, G.M., WILLIAMS, H.M. (2016) Titanium stable isotope investigation of magmatic processes on the Earth and Moon. *Earth and Planetary Science Letters* 449, 197–205.
- MÜNKER, C. (2010) A high field strength element perspective on early lunar differentiation. *Geochimica et Cosmochimica Acta* 74, 7340–7361.
- POITRASSON, F., ZAMBARDI, T., MAGNA, T., NEAL, C.R. (2019) A reassessment of the iron isotope composition of the Moon and its implications for the accretion and differentiation of terrestrial planets. *Geochimica et Cosmochimica Acta* 267, 257–274.
- RAPP, J.F., DRAPER, D.S. (2018) Fractional crystallization of the lunar magma ocean: Updating the dominant paradigm. *Meteoritics & Planetary Science* 53, 1432–1455.
- SCHAUBLE, E.A. (2004) Applying Stable Isotope Fractionation Theory to New Systems. *Reviews in Mineralogy and Geochemistry* 55, 65–111.
- SIMON, S.B., SUTTON, S.R. (2017) Valence of Ti, V, and Cr in Apollo 14 aluminous basalts 14053 and 14072. *Meteoritics & Planetary Science* 52, 2051–2066.
- SNYDER, G.A., TAYLOR, L.A., NEAL, C.R. (1992) A chemical model for generating the sources of mare basalts: Combined equilibrium and fractional crystallization of the lunar magmasphere. *Geochimica et Cosmochimica Acta* 56, 3809–3823.
- SOSSI, P.A., MOYNIER, F. (2017) Chemical and isotopic kinship of iron in the Earth and Moon deduced from the lunar Mg-Suite. *Earth and Planetary Science Letters* 471, 125–135.
- SOSSI, P.A., O'NEILL, H.St.C. (2017) The effect of bonding environment on iron isotope fractionation between minerals at high temperature. *Geochimica et Cosmochimica Acta* 196, 121–143.
- SPRUNG, P., KLEINE, T., SCHERER, E.E. (2013) Isotopic evidence for chondritic Lu/Hf and Sm/Nd of the Moon. *Earth and Planetary Science Letters* 380, 77–87.
- THIEMENS, M.M., SPRUNG, P., FONSECA, R.O.C., LEITZKE, F.P., MÜNKER, C. (2019) Early Moon formation inferred from hafnium–tungsten systematics. *Nature Geoscience* 12, 696–700.
- VAN KAN PARKER, M., MASON, P.R.D., VAN WESTRENNEN, W. (2011) Trace element partitioning between ilmenite, armalcolite and anhydrous silicate melt: Implications for the formation of lunar high-Ti mare basalts. *Geochimica et Cosmochimica Acta* 75, 4179–4193.
- WARREN, P.H., TAYLOR, G.J. (2014) The Moon. *Treatise on Geochemistry (Second Edition)* 2, 213–250.
- WARREN, P.H., WASSON, J.T. (1979) The origin of KREEP. *Reviews of Geophysics* 17, 73.
- WEYER, S., ANBAR, A., BREY, G., MÜNKER, C., MEZGER, K., WOODLAND, A. (2005) Iron isotope fractionation during planetary differentiation. *Earth and Planetary Science Letters* 240, 251–264.

■ Unravelling lunar mantle source processes *via* the Ti isotope composition of lunar basalts

S. Kommescher, R.O.C. Fonseca, F. Kurzweil, M.M. Thiemens, C. Münker, P. Sprung

■ Supplementary Information

The Supplementary Information includes:

- 1. Sample Description
- 2. Methods
- 3. Results
- 4. Discussion
- Tables S-1 to S-7
- Figures S-1 to S-9
- Supplementary Information References

1. Sample description

Table S-1 provides a summary of the petrography and the mineral content of all samples analysed for their stable mass-dependent Ti isotope composition. Detailed sample descriptions and data compilations are available in the lunar sample compendium (Meyer, 2012 and references therein).

2. Methods

2.1. Chemical separation of Ti

For this study, 24 lunar samples collected during the Apollo missions were selected (see Table S-1). High-field strength elements (HFSE), W, U, and Th contents have been determined in a previous study via high-precision isotope dilution MC-ICP-MS (Thiemens *et al.*, 2019). Samples were weighed in Savillex vials, adjusted to contain at least 30 µg of sample Ti and were subsequently spiked in the ideal sample-spike ratio (0.51:0.49). Samples were equilibrated and digested in a concentrated HNO₃:HF (3:1) mixture and placed on a hotplate for 48 hours at 120 °C. After digestion, samples were slowly dried down and refluxed with concentrated HNO₃ and traces of HCl-HF followed by refluxing in 6 M HCl – 0.06 M HF. Prior to column chemistry complete dissolution was verified by visually checking each sample.

Chemical purification of Ti was performed using a three column chemistry following a modified procedure from Münker *et al.* (2001), Bast *et al.* (2015) and Tusch *et al.* (2019). Each sequence consisted of eight lunar samples, two terrestrial reference materials (BCR-2 and JB-2), a chemical reference material (OL-Ti or our newly calibrated in-house reference material Col-Ti), and a



procedural blank. Samples were dissolved in 1 M HCl – 2 % H₂O₂, centrifuged for 10 minutes at 4000 rpm and loaded onto BioRad columns filled with 2 mL AG50W×8 resin (200-400 mesh). Titanium, HFSE, Cr and V are directly eluted during this step. Matrix elements were subsequently eluted with 6 M HCl. In order to avoid dry-down steps, the Ti-HFSE aliquot (1 M HCl – 2 % H₂O₂) is directly loaded onto BioRad columns filled with 2 mL of AG1×8 resin (200-400 mesh). Titanium, Zr, Hf Cr, and V elute directly during the loading step. Tungsten and Mo are subsequently eluted with 6 M HNO₃ – 0.2 M HF – 2 % H₂O₂. Using an LnSpec resin (2 mL resin volume), Ti, Cr and V (loaded and directly collected) were separated from Zr and Hf (subsequently eluted with 2 M HF). To separate Ti from Cr and V, the sample solution is adjusted to a 1 M HF – 0.33 M HCl mixture. After equilibration overnight, samples were loaded onto 120 mL BioRad funnels fitted onto the same BioRad columns filled with 2 mL AG1×8. These columns were cleaned after step two of the chemistry. Chromium and V were directly eluted during loading steps and further eluted in additional 1 M HF – 0.33 M HCl. Titanium was subsequently collected using 1 M HCl – 2 % H₂O₂. At this stage, samples were adjusted again to 1 M HF – 0.33 M HCl and loaded onto the BioRad Columns for a final clean-up. This step was necessary because small amounts of Cr and V in our sample solution were still detectable after the first Cr and V separation step, which decreased the precision of Ti isotope measurements. The purified Ti fraction is finally collected in 6 M HCl – 0.06 M HF. The remaining trace Ti was washed down in 3 M HNO₃ – 0.2 M HF – 2 % H₂O₂. We note that matrix-free samples, such as the OL-Ti reference material, required a slightly higher acid strength on the first column (1.75 M HCl instead of 1 M HCl) to elute Ti with low acid volumes. For matrix-free samples, acid volumes in excess of 30 mL of 1 M HCl – 2 % H₂O₂ (as opposed to the usual 5 mL) are required to elute Ti, because in the absence of any sample matrix Ti is partially adsorbed onto the resin. After Ti purification, samples were dried down and subsequently treated with a 9:1 mixture of 6 M HNO₃ – 0.2 M HF and 30 % H₂O₂ to destroy any remaining organic compounds. After evaporation, samples were re-dissolved in 4 mL 0.3 M HNO₃ – 0.0015 M HF for the measurement of their Ti isotope composition (Millet *et al.*, 2016). Total procedural blanks were always below 10 ng Ti. The blank contribution to sample Ti (*i.e.* >30 µg) was thus considered to be negligible.

2.2 Double Spike calibration and reference materials

We have procured an Alfa Aesar PURATRONIC high-purity Ti rod (99.999 %; LOT. Nr M04C023) to calibrate an in-house reference material similar to the Origins Lab Ti reference material (OL-Ti; Millet *et al.*, 2016; Millet and Dauphas, 2014). The rod was sliced using a diamond string saw and four chips were picked for dissolution into individual stock solutions with varying final Ti concentrations (henceforth called “Col-Ti”). Two high purity ⁴⁷Ti and ⁴⁹Ti oxide powders were obtained from the Oak Ridge National Laboratory. Single spikes and metal chips were weighed in pre-cleaned 250 mL (spikes) and 500 mL (Col-Ti) perfluoroalkoxy alkane (PFA) bottles and dissolved in a 1:19 mixture of concentrated HF and 3 M HNO₃. Titanium spikes were mixed in a 500 mL PFA bottle that had been pre-cleaned with diluted acids over multiple days (diluted HCl, HF, HNO₃ and a HNO₃-HCl mixture) in order to obtain a double spike composition with ⁴⁹Ti/⁴⁷Ti of 1.07207. This optimal value was calculated with the double spike toolbox by Rudge *et al.* (2009). The double spike has a final Ti concentration of 410.9 ± 0.3 µg/g.

Calibration of the double spike was initially performed using an aliquot of OL-Ti, as its isotope composition is well constrained (Millet *et al.*, 2016; Millet and Dauphas, 2014). In order to determine the isotope composition of the double spike, two solutions were prepared: an ideally spiked (sample to spike proportions of 0.51:0.49) aliquot of OL-Ti (1 µg/mL total Ti) and a pure dilution of the double spike (1 µg/mL, pure double spike Ti). Subsequent measurements of the diluted, pure double spike yield average, but not mass-bias-corrected, isotope ratios. Nevertheless, these values should fall on a mass dependent fractionation line with DS-OL-Ti mixture on a three isotope plot. Using the exponential law, we then artificially (*i.e.*, mathematically) fractionated the non-mass-bias-corrected double spike ratios of pure double spike measurements (described above). The corrected ratios are then used in the double spike deconvolution of the doped OL-Ti aliquots. Since the reference material relative to itself is defined as $\delta(^{49}\text{Ti}/^{47}\text{Ti})_{\text{OL-Ti}} = 0 \text{ ‰}$ (henceforth $\delta^{49}\text{Ti}$), the fractionation factor is iteratively adjusted so that the known, average isotope composition of the OL-Ti becomes equal to 0 ‰ (Kurzweil *et al.*, 2018). The isotope compositions of our double spike and in-house reference material correspond to $\delta^{49}\text{Ti}$ of 430 and 0.204 δ -units, respectively. The results are given in Table S-2.

2.3. Validating ideal sample:spike range and Ca-interference correction

In order to verify and better constrain the ideal sample:spike proportion that was calculated using the double spike toolbox of Rudge *et al.* (2009), a set of spiked chemical and terrestrial reference materials were prepared. We prepared aliquots with the equivalent of 30 µg sample Ti of our in-house reference material (36 µL of an 820 µg/mL solution) and added double spike to achieve sample:spike proportions of 0.9:0.1, 0.8:0.2, 0.7:0.3, 0.6:0.4, 0.55:0.45, 0.51:0.49 (ideal ratio) 0.45:0.55, 0.4:0.6, 0.3:0.7, and 0.2:0.8, respectively (see Table S3). Furthermore, eight separate digestions of the reference material BCR-2 (3 mg powder; ~ 30 µg Ti) were spiked in the sample:spike proportions of 0.9:0.1, 0.8:0.2, 0.7:0.2, 0.51:0.49 (ideal ratio), 0.5:0.5, 0.43:0.57, 0.28:0.72, and 0.18:0.82. Lastly, five aliquots of our OL-Ti solution (30 µg Ti), were spiked in the sample:spike proportions of 0.8:0.2, 0.55:0.45, 0.51:0.49 (ideal ratio), 0.45:0.55, and 0.2:0.7. Chemical reference materials were equilibrated in closed vessels over 72 hours and then



diluted for measurement on the MC-ICP-MS. In the case of BCR-2, Ti was separated according to the chemical separation procedure described in Section 2.1.

Our results, shown in Figure S-1 and Table S-3, indicate that for sample:spike proportions between 0.36:0.64 and 0.74:0.26 (a $^{48}\text{Ti}/^{47}\text{Ti}_{\text{Mix}}$ between ~ 1 and ~ 3) $\delta^{49}\text{Ti}$ is accurate. Samples with sample:spike proportions outside this range should be excluded, as delta values drift towards lower values. Except for KREEP-rich sample 68115, all analysed lunar samples and reference materials lie inside the ideal sample:spike range between $^{48}\text{Ti}/^{47}\text{Ti}_{\text{Mix,measured}} = 1.7$ and 3 (Fig. S-1, blue box). Sample 68115 has a $^{48}\text{Ti}/^{47}\text{Ti}_{\text{Mix,measured}}$ of ~ 3.7 . Poorly spiked samples systematically yield lower δ -values, which is not observed in this case. The excellent correlation between $\delta^{49}\text{Ti}$ and the U content of KREEP-rich samples, which indicates the presence of a KREEP-component, supports the notion that the determined Ti isotope composition for 68115 is accurate. In addition, it should be noted that two of our BCR-2 reference materials were poorly spiked with a $^{48}\text{Ti}/^{47}\text{Ti}_{\text{Mix}} \sim 4.9$ and resulting in erroneous values ($\delta^{49}\text{Ti}$, ~ -0.2 ‰ instead of -0.015 ‰), consistent with the calibration tests. The sample:spike proportion in this case would be close to 0.85:0.15.

The isotopes ^{46}Ca and ^{48}Ca interfere with ^{46}Ti and ^{48}Ti , both of which are part of the double spike deconvolution. Accordingly, it is important that the analyte solution is Ca-free, which is usually achieved using the chemical separation procedure described in section 2.1. Nevertheless, the effect of Ca-contamination in the final measurement solution was tested by doping five aliquots (1 $\mu\text{g}/\text{mL}$ Ti) of the spiked Col-Ti solution with an Alfa Aesar Ca plasma standard, resulting in concentrations of 1, 10, 100, 500 and 1000 ng/mL Ca.

Interferences of Ca isotopes can be accurately corrected up to Ca concentrations of 100 $\text{ng}/\mu\text{L}$ or a $^{44}\text{Ca}/^{47}\text{Ti}$ of 0.01 (Fig. S-2a,b) without a significant decrease in the measurement precision of Ti isotope ratios. Larger abundances of Ca cause erroneous, positive $\delta^{49}\text{Ti}$ values. With two exceptions all samples have been measured with an $^{44}\text{Ca}/^{47}\text{Ti}_{\text{measured}}$ below 0.0006. The only two exceptions were samples 15055 and 12022, which displayed $^{44}\text{Ca}/^{47}\text{Ti}_{\text{measured}}$ of 0.0016 and 0.0012, respectively, but still well below the maximum acceptable ratio of 0.01. Given the results of our Ca-interference test, the interferences in our samples are in all cases negligible.

2.4 Ti double spike MC-ICP-MS measurement and data reduction

Each sample was measured using a Thermo Fisher Scientific Neptune Plus at the University of Cologne (Germany) in high-resolution mode with an ESI APEX HF desolvating system and additional glassware fitted after the APEX HF for enhanced signal stability. The machine interface was fitted with a Ni sample- and Ni H-skimmer cone. Sample and additional gas flows, as well as lens settings, were adjusted daily for maximum stability. The resolving power of the instrument determined by the 5 - 95 % peak height is generally in the range of $R = 10,000$. Measured masses were ^{44}Ca , ^{46}Ti , ^{47}Ti , ^{48}Ti , ^{49}Ti , and ^{50}Ti in the L4, L1, C, H1, H2, and H4 cups, respectively. All Faraday cups in the Ti cup configuration were fitted with $10^{11} \Omega$ amplifiers. The isotope ^{44}Ca was used as an interference monitor for ^{46}Ca and ^{48}Ca during measurements. In similar fashion to previous studies, it was assumed that Ca and Ti isotopes fractionate according to the same instrumental mass bias factor (Deng *et al.*, 2018, 2019; Greber *et al.*, 2017b; Millet *et al.*, 2016). Chemical separation of Ca was successful as shown by $^{44}\text{Ca}/^{47}\text{Ti}$ between 2×10^{-3} and 10^{-5} for each sample. All samples contained more than 1 $\mu\text{g}/\text{mL}$ of Ti available for measurement. The instrumental background was determined by measuring the same running solution, which also used to dissolve final samples. This running solution showed intensities for ^{47}Ti , ^{48}Ti and ^{49}Ti in the range of 1, 3 and 1×10^{-14} A, respectively. Samples and standard solutions were measured at intensities of at least 1.5, 2.5 and 1.5×10^{-11} A for the same isotopes. At the start, middle, and end of each measurement sequence a set of spiked OL-Ti and Col-Ti solutions were analysed to monitor eventual drift and gauge long-term precision and accuracy. Furthermore, a spiked in-house Ti standard solution and/or a terrestrial reference material, processed through the chemical separation procedure described above, were measured after each sample for additional quality and accuracy control. Each lunar sample was measured six times including 60 cycles of 8.4 sec integration time each. After each measurement, the wash time was set to 300 sec using a 0.5 M HNO_3 -0.014 M HF-mixture. Double spike deconvolution and, if necessary interference corrections, were performed offline using an iterative method as described in Compston and Oversby (1969), Kurzweil *et al.* (2018) and Schönberg *et al.* (2008).

2.5 Precision and accuracy

Samples were also measured using the standard-sample bracketing technique to account for possible unresolved polyatomic interferences and for additional quality control and drift monitoring, in addition to mass-bias correction using the double-spike method. The intermediate precision of these measurements is depicted in Figure S-3. The best gauge for the precision of our method is the long-term variation of values obtained for terrestrial reference materials (twice the standard deviation, henceforth s), which is always better than 0.023 ‰. Intermediate precision (2 s.d.) of both Col-Ti and OL-Ti are better than 0.021 ‰ (2 s.d.). Results for processed reference materials JB-2 and BCR-2 are -0.044 ± 0.023 ‰ (2 s.d., $n = 7$ sequences) and -0.025 ± 0.012 ‰ (2 s.d., $n = 4$ sequences), respectively. Both terrestrial reference materials were processed three times and measured between six to 12 times



during each sequence. Ideally spiked JB-2 and BCR-2 reproduce previously reported values (Deng *et al.*, 2018, 2019; Greber *et al.*, 2017b, 2017a; Millet *et al.*, 2016). Two aliquots of BCR-2 were poorly spiked having a sample:spike proportions of 0.85:0.15 rather than the optimal 0.51:0.49 (calculated with the *double spike toolbox*; Rudge *et al.*, 2009). These BCR-2 measurements resulted in erroneously low $\delta^{49}\text{Ti}$ values of $\sim -0.2\text{‰}$, which is consistent with our results of standard measurements with sample:spike ratios outside the optimal range (described in section 2.3). Chemically processed OL-Ti and Col-Ti reference materials are identical to their pure, unprocessed counterparts (Fig. S-1, Table 1 in the manuscript).

2.6 Neutron capture effects and potential sampling bias

Inasmuch as the Ti isotope analyses of lunar samples is concerned, secondary neutron capture effects due to the long-term exposure to cosmic rays can be an issue, and this possibility needs to be addressed (see also: Sprung *et al.*, 2013). Moreover, potential sampling bias due to small processed sample quantities may occur, which would lessen the representability of any reported $\delta^{49}\text{Ti}$ values. What follows is a discussion of what has been done to investigate these issues and what steps, if any, were taken to mitigate them.

We evaluated the effect of neutron capture on Ti isotopes using thermal neutron capture cross sections and epithermal resonance integrals calculated as described in Sprung *et al.* (2010, 2013) and using the JENDL 3.3 pointwise library at 300 K. Including these values and Ca/Ti, as well as Sc/Ti from Meyer (2012), into the neutron capture model of Sprung *et al.* (2010, 2013) it becomes clear that the dominant process is the production of ^{49}Ti via neutron capture by ^{48}Ti . Thus, the dominant effect of neutron capture on Ti isotope ratios referenced to ^{47}Ti is an increase of $^{49}\text{Ti}/^{47}\text{Ti}$, which is commonly used for mass bias correction. For samples that are strongly affected by neutron capture, the mass bias corrected ratios of ^{50}Ti , ^{48}Ti , and ^{46}Ti normalized to ^{47}Ti should display coupled anomalies. The magnitudes of such anomalies are expected to scale with the mass difference to ^{47}Ti because of erroneously addressing the neutron capture-induced shift in $^{49}\text{Ti}/^{47}\text{Ti}$ to mass bias. For example, neutron capture effects on Ti in lunar rocks have been reported primarily for ^{50}Ti (Gerber *et al.*, 2017; Trinquier *et al.*, 2009; Zhang *et al.*, 2012) whose mass differs the most from ^{47}Ti . From our evaluation, we conclude that the *true* neutron capture-induced anomalies in $^{46}\text{Ti}/^{47}\text{Ti}$ and $^{48}\text{Ti}/^{47}\text{Ti}$, which are used in the double spike deconvolution (Greber *et al.*, 2017b) are at least one order magnitude lower than the (artificial) anomaly observed in $^{50}\text{Ti}/^{47}\text{Ti}$, while in $^{49}\text{Ti}/^{47}\text{Ti}$ they are ca. 1.5 times lower. Judging from the available data for lunar rocks (Gerber *et al.*, 2017; Trinquier *et al.*, 2009; Zhang *et al.*, 2012), no significant effects outside of our measurement reproducibility are expected, even for more strongly neutron-irradiated samples such as low-Ti mare basalt 15556 (*i.e.*, Sprung *et al.*, 2013; See Figure S 4 b). The lack of any observable correlation between $\delta^{49}\text{Ti}$ and $\mu^{180}\text{Hf}$, which is a known monitor for epithermal neutron, or with other proxies for prolonged cosmic-ray-exposure (exposure age data *e.g.*, Meyer, 2012; *e.g.*, $\epsilon^{149}\text{Sm}$, Sprung *et al.*, 2013; See Figure S 4 b) supports this conclusion. A similar assertion was reached for lunar samples using the Ti double spike method (Greber *et al.*, 2017b; Mandl *et al.*, 2018).

Regarding sampling bias, sample weights in this study range from 3 to 10 mg and were taken from ~ 0.5 g powdered aliquots. The primary Ti phase in all relevant samples is ilmenite, whose crystallisation is thought to be the foremost process fractionating Ti isotopes (Millet *et al.*, 2016). The absence of any clear correlation between $\delta^{49}\text{Ti}$, SiO_2 , and TiO_2 content, or with the modal abundance of Fe-Ti oxides reported for each sample, indicates that the sample $\delta^{49}\text{Ti}$ is independent of ilmenite (and TiO_2) content (Fig. S-4a). Consequently, sampling bias is unlikely to have affected our $\delta^{49}\text{Ti}$ results.

3. Results

Unless otherwise stated, all uncertainties in this sub-chapter are always refer to 95 % confidence intervals (see also Table 1 and Fig. 1 in the manuscript). All results are given as $\delta(^{49}\text{Ti}/^{47}\text{Ti})_{\text{OL-Ti}}$, *i.e.*, the deviation of the $^{49}\text{Ti}/^{47}\text{Ti}$ ratio of the sample relative to the OL-Ti reference material in permil (‰), henceforth referred to simply as $\delta^{49}\text{Ti}$. The Ti stable isotope composition for 24 analysed lunar samples ranges from $-0.030 \pm 0.007\text{‰}$ (15065, low-Ti quartz-normative basalt) to up to $+0.296 \pm 0.016\text{‰}$ (14305, KREEP-rich breccia). The $\delta^{49}\text{Ti}$ of low-Ti mare basalts ranges between -0.030 ± 0.007 and $+0.055 \pm 0.012\text{‰}$ (12063, low-Ti ilmenite basalt), but their average $\delta^{49}\text{Ti}$ is identical with the bulk silicate Earth (BSE, $\delta^{49}\text{Ti} = +0.005 \pm 0.005\text{‰}$) value determined by Millet *et al.* (2016). All Apollo 11 high-Ti ilmenite basalts are identical to this BSE-value as well. However, Apollo 17 high-Ti samples (breccias and ilmenite basalts) show resolved positive $\delta^{49}\text{Ti}$ between $+0.019 \pm 0.009$ (79135, high-Ti breccia), and $+0.047 \pm 0.010\text{‰}$ (79035, high-Ti breccia). Apollo 17 high-Ti ilmenite basalt 75035 shows the highest recorded $\delta^{49}\text{Ti}$ for this sub-set of samples, with a value of $+0.115 \pm 0.013\text{‰}$. The average value for $\delta^{49}\text{Ti}$ of the high-Ti basalt suite overlaps with that of BSE, but is offset to higher values, especially when 75035 is not considered an outlier and is included into the high-Ti average. KREEP-rich samples span a range of $\delta^{49}\text{Ti}$ between $+0.117 \pm 0.014$ (KREEP-rich breccia 68115) and $+0.296 \pm 0.016\text{‰}$ (KREEP-rich breccia 14305). The highest observed $\delta^{49}\text{Ti}$ for KREEP-rich samples ($+0.296 \pm 0.016\text{‰}$) is identical, within uncertainty, to the value obtained for lunar meteorite Sayh al Uhaymir (SaU 169; $+0.330 \pm 0.034\text{‰}$), which is thought to represent KREEP (Greber *et al.*, 2017b).



Except for Apollo 16 KREEP-rich breccia 68115, the $\delta^{49}\text{Ti}$ of KREEP-rich samples show a positive correlation with SiO_2 , MgO , FeO , and TiO_2 content, as well as with incompatible trace elements like U and Th. In non-KREEP samples, no positive correlation between $\delta^{49}\text{Ti}$ and SiO_2 , MgO , FeO , or TiO_2 content is observed. However, $\delta^{49}\text{Ti}$ shows a negative correlation with MgO/TiO_2 , suggesting that it may relate to ilmenite crystallisation (see manuscript for discussion). Samples with low MgO/TiO_2 display higher $\delta^{49}\text{Ti}$ than samples with increasing MgO/TiO_2 . There is no further co-variation between Ti isotope composition of non-KREEP samples and their Zr, Nb, W, Hf, or U contents. However, ratios between compatible and incompatible HFSE (*i.e.*, Ta/Hf or Nb/Zr – see partitioning data from Leitzke *et al.*, 2016, 2017 and Table S-6) allow the distinction of several sample groups, seemingly connected through a first negative, then positive correlation of $\delta^{49}\text{Ti}$ with increasing Ta/Hf (see Fig. 2b in the manuscript). The Apollo 12 low-Ti samples show the lowest observed Ta/Hf between 0.0837 and 0.119 and positive $\delta^{49}\text{Ti}$ between +0.029 and +0.055 ‰. Apollo 15, Apollo 11 samples and the Apollo 12 non-ilmenite basalts (olivine-normative basalts and quartz-normative basalts, ONB and QNB, respectively) have $\delta^{49}\text{Ti}$ between +0.011 and –0.030 ‰ and Ta/Hf between 0.124 to 0.148. Samples with higher Ta/Hf (Apollo 17 breccias and ilmenite basalts, Ta/Hf between 0.154 and 0.175), exhibit higher $\delta^{49}\text{Ti}$ values between +0.010 and +0.116 ‰. The same groups can be distinguished when using Nb/Zr. For a detailed discussion of the HFSE data set for these samples the reader is referred to Thiemens *et al.* (2019).

4. Discussion

4.1 Experimental constrains on the petrogenesis of lunar samples

Longhi (1992) and Shearer (2006) give excellent literature overviews of experimental petrology research of lunar samples. In this section, we will briefly summarize findings relevant for the interpretation of our data.

Walker *et al.* (1977) argued that low-Ti ONB 15555 formed as a result of melting from a source region at around 170 km depth. Crystallisation experiments of a 15555-like composition shows that ilmenite does not appear along its liquid line of descent as a liquidus phase (Kesson, 1975). In absence of a Ti-bearing phase, no significant fractionation of Ti isotopes should take place (Millet *et al.*, 2016; assuming ilmenite or armacolite are the only phases fractionating Ti isotopes), which is consistent with our own results where $\delta^{49}\text{Ti}$ is the same as that of BSE within analytical uncertainty (*i.e.*, ca. 0 ‰). Low-Ti QNB 15065 is thought to have originated from shallower regions of the lunar mantle of above 100 km (Walker *et al.*, 1977). At these depths, Kesson (1975 and references therein) suggested that low-Ti magmas assimilated a portion of an ilmenite-bearing cumulate (IBC) to form a high-Ti basalt. The bulk assimilation of IBC by a low-Ti magma would result in this magma inheriting the Ti isotopic composition of the IBC. Modelling suggests that, depending on the timing IBC formation from the LMO, the Ti isotopic composition of the IBC would range between –0.4 and –0.2 ‰ (very early crystallised ilmenite, depending on accuracy of ilmenite/melt fractionation factor of Johnson *et al.*, 2019 or; Millet *et al.*, 2016) or close to 0 ‰ (very late crystallised ilmenite). Results from experiments carried out using compositions akin to low-Ti quartz-normative basalt 15065 also shows no evidence for fractional crystallisation of ilmenite, meaning the variations observed in the $\delta^{49}\text{Ti}$ of our QNB samples could be ascribed to source heterogeneity. Crystallisation experiments show that in low-Ti ilmenite basalt 12022 ilmenite is among the first phases appear on the liquidus (Green *et al.*, 1971), which would induce Ti isotope fractionation. Green *et al.* (1975 and references therein) report that most Apollo 17 high-Ti basalts have around 10 % ilmenite as a liquidus phase, which can potentially indicate $\delta^{49}\text{Ti}$ fractionation in some high-Ti mare basalts due to ilmenite crystallisation.

The source region of Apollo 11 and 17 high-Ti mare basalts is at an estimated depth of 250 km (Delano and Lindsley, 1982). Based on high MgO/FeO , high K/Rb, and experimental results, Shih *et al.* (1975 and references therein) assume that Apollo 11 and 17 high-Ti mare basalts evolved from a parent magma similar in composition to Apollo 17 sample 70017. The analysed suite of Apollo 11 and 17 basalts compositions is accurately reproduced by partial melting modelling. In detail, high-Ti mare basalts compositions of 75035, 74255 and 74275 are reproduced by Shih *et al.* (1975) assuming partial melting (equilibrium melting) of a mantle source with 90 % cpx and 10 % ol+ilm (75035) and 70 % cpx and 30 % ol+ilm (74255, 74275). Based on this model Apollo 11 and 17 low-K high-Ti basalts (*e.g.*, 10020 and 75035) are the result of 20 % partial melting, whereas Apollo 11 high-K basalts (10017 and 10057) result from around 1 % partial melting. Partial melting of ilmenite-bearing domains is expected to lead to more fractionated Ti isotope compositions in the melt (*i.e.*, higher $\delta^{49}\text{Ti}$), especially if ilmenite remains a residual phase throughout melting.

4.2 Modelling the Ti isotope composition of urKREEP

The co-genetic relationship between urKREEP and IBC permits studying the $\delta^{49}\text{Ti}$ evolution of both reservoirs. UrKREEP represents the last vestige of the LMO prior to its full crystallization (Warren and Wasson, 1979), and is expected to have developed higher $\delta^{49}\text{Ti}$ due to the prior crystallization of the IBC (Greber *et al.*, 2017b; Millet *et al.*, 2016). Two different approaches have been



used to constrain the Ti isotope composition of the pristine urKREEP-component. We have taken advantage of pre-existing high-precision HFSE, U, Th and W data by Thiemens *et al.* (2019) for the same samples studied here. UrKREEP is enriched in incompatible elements like U and Th, whereas Ti, Hf, and Zr are preferentially incorporated into ilmenite, and are therefore expected to have fractionated into the IBC (Gross and Joy, 2016; Münker, 2010; Snyder *et al.*, 1992). Therefore, the U/Ti, U/Hf and U/Zr should be highest in the pristine urKREEP component assuming its coeval formation with the IBC. Moreover, urKREEP should also have the highest $\delta^{49}\text{Ti}$ due to the contemporaneous extraction of lighter Ti isotopes into the IBC (Greber *et al.*, 2017b; Millet *et al.*, 2016). This expectation was met by lunar meteorite SaU 169, which is thought to represent urKREEP, and has an $\delta^{49}\text{Ti}$ of $+0.330 \pm 0.034$ ‰ (Greber *et al.*, 2017b). Our two KREEP-rich samples with the highest U/Ti, U/Hf and U/Zr (14310 and 14305) yield $\delta^{49}\text{Ti}$ of $+0.263 \pm 0.018$ and $+0.296 \pm 0.016$ ‰ values that are very similar to those reported for SaU 169 (Greber *et al.*, 2017b). Furthermore, estimates for U/Ti, U/Hf and U/Zr by Warren and Taylor (2014) show that 14305 and 14310 fall well within the estimated range of these ratios for urKREEP (Fig. S-5a-c). The same can be shown for SaU 169 using trace-element data by Gnos *et al.* (2004). Assuming our KREEP-rich samples and SaU 169 are in the same range as the U/Zr of the pristine urKREEP-component, our modelling results in a value for $\delta^{49}\text{Ti}_{\text{urKREEP}}$ of $+0.296 \pm 0.067$ ‰ (propagated uncertainty).

In a second approach, we have modelled the evolution of the $\delta^{49}\text{Ti}$ of the LMO, and its Ti, Hf and Ta concentration, as it crystallises. Millet *et al.* (2016) assumed all mass-dependent Ti isotope fractionation occurs in the last stages of LMO crystallisation once the solidus of ilmenite is reached. The different LMO crystallisation models predict different mineral assemblages but all share a common, late stage ilmenite crystallisation phase (Charlier *et al.*, 2018; Elkins-Tanton *et al.*, 2011; Lin *et al.*, 2017; Rapp and Draper, 2018; Snyder *et al.*, 1992; Wang *et al.*, 2015; Table S-5).

However, silicate minerals, mainly pyroxenes (clino- and orthopyroxene and pigeonite), can also incorporate Ti, causing variations in its bulk partition coefficient ($D_{\text{Ti}}^{\text{bulk/melt}}$) during LMO crystallisation. Whatever role these phases may play in fractionating Ti isotopes is currently unknown and merits further study; however, Johnson *et al.* (2019) have recently suggested silicates have little to no influence on the Ti isotope composition of lavas from Kilauea Iki lava lake. This view has been reinforced by recent *ab initio* modelling by Wang *et al.* (2019) who found no evidence that substitution of tetravalent Ti in clino- and orthopyroxene results in significant mass-dependent Ti isotope fractionation. Therefore, and as in previous studies, we will assume that the bulk of the Ti isotope fractionation in the LMO during crystallisation is ilmenite-controlled (following Millet *et al.*, 2016). As such, prior to ilmenite saturation, the $\delta^{49}\text{Ti}$ of the LMO will be assumed to be 0 ‰.

Rapp and Draper (2018) include large fractions of clinopyroxene in their experimentally-constrained model starting from around 75 % solidification (between 35 % and 50 %). Titanium is weakly incompatible into clinopyroxene in its tetravalent form, with $D_{\text{Ti}}^{\text{cpx/melt}}$ of ~0.2 (Mallmann and O'Neill, 2009; Leitzke *et al.*, 2016). However, at more reduced lunar $f\text{O}_2$, Ti^{3+} is also present, which is compatible in clinopyroxene with a $D_{\text{Ti}}^{\text{cpx/melt}} \sim 1$ (Leitzke *et al.*, 2018; Mallmann and O'Neill, 2009). As such, the potential presence of Ti^{3+} needs to be considered when assessing the partitioning behaviour of Ti during LMO crystallisation. Using recent mineral/melt partition data from Leitzke *et al.* (2016), the concentrations of Ti, Hf, Zr, and Ta in the mineral assemblage and the residual liquid can be calculated assuming fractional crystallisation with $C_s = C_0 \cdot DX_l^{(D-1)}$ and $C_l = C_0 \cdot X_l^{(D-1)}$. In these equations, $C_{s,l,0}$ are the concentrations of the modelled element in the solid, liquid and the initial LMO (Snyder *et al.*, 1992), D is its bulk mineral/melt partition coefficient, and X_l the liquid that remains after each LMO crystallisation step. Snyder *et al.* (1992) do not include Ta in their model, but Münker (2010) calculated Ta contents based on the Nb content given in Snyder *et al.* (1992) and a Nb/Ta of 17. In addition, Snyder *et al.* (1992) do not provide a partition coefficient for Ta in pigeonite as they model Nb instead. In this case, we use Ta partitioning data for a pigeonite-like pyroxene published by van Westrenen *et al.* (2000). With ilmenite at liquidus, the bulk solid-melt fractionation factor for Ti ($\Delta T_{i_{\text{solid-melt}}}$) should be almost equal to the oxide-melt fractionation factor ($\Delta T_{i_{\text{oxide-melt}}}$). The Ti isotope composition can then be calculated using a simple Rayleigh distillation model:

$$\Delta T_{i_{\text{solid-melt}}} \approx \Delta T_{i_{\text{oxide-melt}}} = -0.23 \cdot 10^6 / T_2 \quad (\text{Eq. S-1})$$

$$\Delta T_{i_{\text{oxide-melt}}} = 1000 \cdot \ln(\alpha) \quad (\text{Eq. S-2})$$

$$\frac{R_X}{R_0} = \left(\frac{X_l}{X_0} \right)^{(\alpha-1)} \quad (\text{Eq. S-3})$$

Partition coefficients were selected so that the Ti content (~10 % TiO_2), the oxygen fugacity ($f\text{O}_2$, ~IW -1.6) and the temperature of the experiments they derived from (~1500 K, 100 K higher than in Millet *et al.* (2016)), appropriately reflected the conditions prevalent during LMO crystallisation (Leitzke *et al.*, 2016). To calculate the proportion of Ti^{3+} in the minerals that crystallise from the LMO, we have used the experimental dataset of Mallmann and O'Neill (2009), who determined mineral/melt



partition coefficients for Ti over a wide range of fO_2 (see Table S-6 for an overview of the values used).

The modelled $\delta^{49}\text{Ti}$ shows that late-stage ilmenite crystallisation causes a sharp increase in the $\delta^{49}\text{Ti}$ of the melt that remains in the LMO – *i.e.*, KREEP (Fig. S-6a-d). Considering the estimate for Ti, Hf, and Ta in the urKREEP component by Warren and Taylor (2014) and Warren and Wasson (1979), the $\delta^{49}\text{Ti}$ of the melt at those concentrations should reflect $\delta^{49}\text{Ti}_{\text{urKREEP}}$. The intersect between the minimum, average and maximum Ti, Hf and Ta concentrations in urKREEP (Warren and Taylor, 2014), and our modelled $\delta^{49}\text{Ti}_{\text{urKREEP}}$ evolution result in $\delta^{49}\text{Ti}_{\text{urKREEP}}$ of $+0.26 \pm 0.10$ ‰, $+0.29 \pm 0.07$ ‰ and 0.31 ± 0.05 ‰, respectively. These values can be used to constrain the Ti isotope composition of the complementary IBC, which results in a $\delta^{49}\text{Ti}_{\text{IBC}}$ of -0.010 ± 0.013 ‰, -0.0075 ± 0.0062 ‰ and -0.0060 ± 0.0034 ‰, respectively. These values are reached (on average) after 98%, 99%, and 99.2% solidification. Titanium isotope compositions calculated using the LMO crystallisation models by Snyder *et al.* (1992), Lin *et al.* (2017), Charlier *et al.* (2018), and Rapp & Draper (2018) all result in $\delta^{49}\text{Ti}$ values for KREEP that are consistent with what was estimated here, and what has been measured in KREEP-rich samples (Greber *et al.* 2017b; this study).

It is worth mentioning that the model of Elkins-Tanton *et al.* (2011, not shown) results in $\delta^{49}\text{Ti}$ that are 0.1 δ -units too low compared to the actual KREEP value. Only modifying their oxide assemblage to 100% ilmenite, *i.e.*, 10% of ilmenite in the bulk mineral assemblage, produces values identical to those produced from other LMO crystallisation models, which is an unrealistic expectation. Furthermore, models including trivalent Ti show significant differences during mid- to late-stage clinopyroxene-crystallisation. However, with no specific Ti^{3+} -isotope-fractionation factor available, we had to assume the same bulk solid-melt isotope fractionation factor used in the Rayleigh model for Ti^{3+} and Ti^{4+} . The effect of variable amounts of Ti^{3+} and Ti^{4+} is expected to be of secondary importance as soon as ilmenite appears on the LMO liquidus. Wang *et al.* (2019) however performed first-principle calculations to constrain Ti isotope fractionation factors for a range of mineral-compositions and report enrichment of light Ti isotopes in Ti^{3+} -bearing pyroxene relative to Ti^{4+} -bearing pyroxenes of up to 1 δ -unit. The determination of the real Ti^{3+} -isotope-fractionation factor is consequently indispensable in order to better discuss the distinct Ti isotope effects expected for different LMO crystallisation models.

4.3 Modelling the Ti isotope evolution of mare basalts

Several petrogenetic processes can potentially lead to the variations in $\delta^{49}\text{Ti}$ seen in our low- and high-Ti basalt samples. These processes include: 1) partial melting of IBC, or of an hybridised mantle source in the presence of residual ilmenite; 2) fractional crystallization of ilmenite from a mare basaltic magma; 3) bulk assimilation of IBC, assimilation of IBC followed by fractional crystallization; 4) Mixing between IBC partial melts and a low-Ti magma (*e.g.*, Longhi, 1992; Warren and Taylor, 2014 and references therein). In the following, we model the how the Ti, Hf, Ta concentrations in a mare basalts and its Ti isotope composition may change as a result of each of these processes.

Low-Ti mare basalts: Mid- to late-stage cumulates, *i.e.*, (olivine-) pyroxenites (Green *et al.*, 1971; Longhi, 1992) are the inferred source for partial melts that eventually produce low-Ti mare basalts (corresponding to around 50 % - 90 % percent solidification (PCS) found in Charlier *et al.*, 2018; Lin *et al.*, 2017; Rapp and Draper, 2018; Snyder *et al.*, 1992). The concentration of an element in the cumulate (fractional crystallisation, C_s) can be calculated by $C_s = C_0 \cdot DX_l^{(D-1)}$. We then use an aggregate modal fractional melting model (Shaw, 1970) to create a partial melt from this cumulate composition. At low degrees of partial melting (between 5 % and 35 %; Binder, 1985), we model the fractional crystallisation of ilmenite, with a crystallising mineral assemblage modelled after Apollo 12 low-Ti ilmenite basalt 12063 (10% olivine, 60 % orthopyroxene, 20 % plagioclase and 10 % opaques = ilmenite; Meyer, 2012). Before the occurrence of ilmenite, 99 – 80 % of the total Ti still remains in the melt and determines its isotope composition. As such, the absence of ilmenite leads us to assume an unfractionated Ti isotope composition of the ilmenite-free cumulate (*i.e.*, before ilmenite occurrence $\delta^{49}\text{Ti}_{\text{cumulate}} = 0$ ‰, see also Millet *et al.*, 2016; and Wang *et al.*, 2019).

Fractional crystallisation of ilmenite produces a negative, near vertical covariation of $\delta^{49}\text{Ti}$ with Ta/Hf in a low-Ti melt (Fig. S-7a). However, the partial melt results in a very low Ta/Hf of ~ 0.05 and it is not possible to accurately reproduce our samples in a single or two stage model from this composition. Increasing the degree of partial melting barely affects the Ta/Hf of the partial melt, as the cumulate itself contains little to no Ta or Hf. We tested all other cumulate compositions from the different LMO crystallization models (Charlier *et al.*, 2018; Lin *et al.*, 2017; Rapp and Draper, 2018; Snyder *et al.*, 1992), and all models resulted in Ta/Hf well below the observed range of Ta/Hf in lunar mare basalts. However, once the cumulate is assumed to contain ilmenite (> 95 % PCS), the Ta/Hf of the resulting partial melt becomes fractionated from its source, due to the higher compatibility of these elements into ilmenite. In this case, the modelled evolution of $\delta^{49}\text{Ti}_{\text{melt}}$, and especially Ta/Hf_{melt}, is consistent with observed values. However, the notion that the low-Ti source could contain ilmenite is not supported by previous studies (Green *et al.*, 1971; Kesson and Ringwood, 1976; Longhi, 1992), and thus a different approach is necessary. If our most primitive sample, the low-Ti mare basalt 12004, represents the ambient lunar mantle composition, then its Ta, Hf and Ti contents may be used as a source composition in this model. The liquid generated from partial melting of this source composition (15 to 35 % melting of an assemblage of 90% PCS Charlier *et al.* (2018): 20 % clinopyroxene, 48 % plagioclase and 32 % pigeonite) is then used in a fractional crystallisation



model. Fractional crystallisation of minerals in a composition of Apollo 12 low-Ti ilmenite basalt 12063 (10% olivine, 60 % orthopyroxene, 20 % plagioclase and 10 % opaques = ilmenite; Meyer, 2012) results in a decreasing Ta/Hf_{melt} as the $\delta^{49}\text{Ti}_{\text{melt}}$ increases. The 12004-like source composition accurately reproduces the observed $\delta^{49}\text{Ti}$ and Ta/Hf in our analysed low-Ti ilmenite basalts (Fig. S-7a). This suggests that the Apollo 12 sample 12004 is closer in its HFSE and Ti isotope composition to the source composition of our low-Ti samples than the modelled cumulate compositions. It also suggests that the variations in $\delta^{49}\text{Ti}$ in our low-Ti ilmenite basalts most likely stem from the fractional crystallisation of ilmenite. It is thus also possible to use low-Ti mare basalt 12004 as a reference-point regarding fractional crystallisation of ilmenite in low-Ti mare basalts.

High-Ti mare basalts: Ringwood (1970) reports that Apollo 11 basalts most probably result from the partial melting of an IBC component, which is supported by Shih *et al.* (1975 and references therein). Based on main- and trace elements constraints, Shih *et al.* (1975) use the composition of (ilmenite-bearing) Apollo 17 sample 70017 as the initial liquid composition. The more evolved Apollo 11 and Apollo 17 high-Ti mare basalt compositions are then accurately reproduced by a partial melting model. Estimated degrees of partial melting are between ~ 5 % and more than 20 %, respectively (Binder, 1985; Shih *et al.*, 1975). In order to investigate the partial melting of the IBC, and its effect on the Ti isotope composition and the Ta/Hf of the resulting melt and residue, we used the same source composition and proposed mineral modes utilized by Shih *et al.* (1975), coupled with the mineral partitioning dataset from Leitzke *et al.* (2016; consistent with *e.g.*, van Kan Parker *et al.*, 2011) and van Westrenen *et al.* (2000; for pigeonite). As before, we have also assumed the same fractionation factor for Ti isotopes used by Millet *et al.* (2016) (see Equations S-1 to S-3), and degrees of melting consistent with previous studies (1 to 25 % melting).

Applying an aggregate fractional melting model to the composition of (ilmenite-bearing) Apollo 17 sample 70017 (similar to Shih *et al.*, 1975), we observe a steady increase in Ta/Hf with degree of partial melting, and a positive covariation between Ta/Hf and $\delta^{49}\text{Ti}$ in the melt. Most of our sample compositions can be reproduced within degrees of partial melting consistent with what was proposed by Shih *et al.* (1975) and by Binder (1985) in this single stage approach (between 5 and 25 % melting - Figure S7 b). The positive covariation of $\delta^{49}\text{Ti}$ and Ta/Hf, estimated degrees of partial melting (Shih *et al.*, 1975), as well as our model results, strongly support a petrogenesis by partial melting of an ilmenite-rich source (Figure S7 b). This possibility is also consistent with the modelled depth of the deep source for high-Ti mare basalts 74275 and 74255 (~250 km; Delano and Lindsley, 1982). Petrographic evidence for early fractional crystallisation of ilmenite (large laths of ilmenite penetrating most other minerals; Meyer, 2012 and references therein) in Apollo 17 sample 75035 may be reconciled by a combination of partial melting and fractional crystallisation: Partial melting (ca. 25 %) of a source with the 70017-like composition results in a liquid with a $\delta^{49}\text{Ti}$ value of ~ 0.04 ‰ and a Ta/Hf of ~ 0.18. Subsequent fractional crystallisation of ilmenite (crystallising mineral assemblage: 15 % olivine, 70 % clinopyroxene and 15 % ilmenite) from this melt composition can accurately reproduce the observed $\delta^{49}\text{Ti}$ and Ta/Hf of Apollo 17 sample 75035 (after 50 - 60 % fractional crystallisation). This can reconcile the partial melting origin (Shih *et al.*, 1975) and the observations that ilmenite is often a near-liquidus phase in high-Ti mare basalts (Longhi, 1992 and references therein) with our $\delta^{49}\text{Ti}$ and Ta/Hf data. It is nevertheless evident that based on our results and modelling, IBC partial melting plays a major role in high-Ti mare basalt petrogenesis (*e.g.*, 74275 and 74255). It should also be noted that these trends are mostly constrained by their source composition, which in this case corresponds to that of Apollo 17 sample 70017. It is however possible to model the partial melting of the different ilmenite-bearing cumulates from the LMO models.

4.4 Partial melting of different cumulate compositions

Inasmuch as the evolution of $\delta^{49}\text{Ti}_{\text{urKREEP}}$ is concerned, the models by Snyder *et al.* (1992), Lin *et al.* (2017), Charlier *et al.* (2018), and Rapp & Draper (2018) all result in Ti isotope compositions that agree well with our conclusions and those from previous studies (Greber *et al.*, 2017b; Millet *et al.*, 2016). We have shown in the previous chapter that partial melting of late-stage ilmenite-bearing cumulates likely plays a key role in high-Ti mare basalt petrogenesis (*e.g.*, Shih *et al.*, 1975; Sossi and Moynier, 2017). We now constrain how partial melting of the different late stage IBC compositions, as produced by the different LMO solidification models, affects the $\delta^{49}\text{Ti}_{\text{melt}}$ and Ta/Hf_{melt} of the melt. Like in 4.2 and 4.3, we have used partition coefficients by Leitzke *et al.* (2016) and van Westrenen *et al.* (2000; for pigeonite), the petrogenetic source composition of the ilmenite-bearing cumulate at 99 % PCS of each LMO crystallization model and the calculated Ti, Hf, and Ta concentrations. With ilmenite now present, the Ti isotope composition of the IBC for each model can be constrained with:

$$R_{X,\text{cumulate}} = R_0 / \left(\frac{X_{\text{cumulate}}}{X_0} \right)^{(\alpha-1)} \quad (\text{Eq. S-4})$$

The $\delta^{49}\text{Ti}_{\text{modelled}}$ versus Ta/Hf_{modelled} for each LMO solidification model is shown in Figure S-8. Results obtained using the Snyder *et al.* (1992) model yield the minimum values for $\delta^{49}\text{Ti}_{\text{melt}}$, Ta/Hf_{melt}, whereas the Rapp and Draper (2018) result in the maximum values for $\delta^{49}\text{Ti}_{\text{melt}}$ and Ta/Hf_{melt}. The Charlier *et al.* (2018) model and the Lin *et al.* (2017) model overlap during the entirety of the evolution and evolve from Ta/Hf_{melt} lower than that predicted with the Snyder *et al.* (1992) model to higher Ta/Hf_{melt}



at the same $\delta^{49}\text{Ti}_{\text{melt}}$. The evolution line calculated assuming the Rapp and Draper (2018) LMO evolution model fits best with most samples: The two high-K high-Ti Apollo 11 basalts intersect with the Rapp and Draper (2018) model between 5 and 10 % partial melting, which is consistent with results by Shih *et al.* (1975). Most of our Apollo 17 high-Ti samples are reproduced by the Rapp and Draper (2018) model curve at 10 – 20 % partial melting, while the $\delta^{49}\text{Ti}$ and Ta/Hf of Apollo 17 high-Ti basalt 75035 is reached at around 50 % of partial melting. These results reinforce the notion that the high-Ti mare basalts analysed in this study are the products of partial melting of the IBC in the presence of residual ilmenite, and that the variations in $\delta^{49}\text{Ti}$ and Ta/Hf can potentially be explained with partial melting alone.

4.5 Assimilation of an IBC component by a low-Ti magma

While the TiO_2 contents in our Apollo 15 samples are too low to be consistent with the assimilation of IBC during fractional crystallisation, it is worth investigating this process in light of high-Ti mare basalt petrogenesis. Three approaches are used to constrain the admixing of an IBC component into a low-Ti magma: Bulk addition of a portion of an IBC into a low-Ti magma, assimilation-fractional crystallisation (henceforth AFC, described in DePaolo, 1981), and mixing of an 12004-derived magma with an IBC-derived magma. Kesson and Ringwood (1976) mention that in order to reach the TiO_2 contents found in high-Ti mare basalts, the low-Ti parental magma would need to assimilate up to 60 % of IBC material. The authors further point out that this range of AFC is problematic because the high-Ti basalt parental magma would need experience up to 40 – 45 % of fractional crystallisation in order to produce the required heat to drive wall-rock assimilation, which is hard to reconcile with the Mg# and Cr-contents of high-Ti mare basalts. In section 4.3 we pointed out that using the composition of our most primitive low-Ti sample (12004), in lieu of a modelled cumulate, accurately reproduces our low-Ti ilmenite basalts. For both AFC and bulk addition, we will use a liquid produced from the modelled cumulate (90 % PCS; Charlier *et al.*, 2018). In addition, the same mineral assemblage as 90 % PCS Charlier *et al.* (2018), but with a 12004-like trace element composition will be used to model the same processes. Millet *et al.* (2016) constrain a Ti isotope composition of these late stage IBC components between $\delta^{49}\text{Ti}_{\text{cumulate}} = -0.1 \text{ ‰}$ and $\sim 0 \text{ ‰}$. With the onset of ilmenite crystallisation all our models initially result in $\delta^{49}\text{Ti}$ above the Millet *et al.* (2016) estimate of -0.06 ‰ to -0.01 ‰ , which is likely due to the different model approaches. Specifically, while Millet *et al.* (2016) assume that at the point of ilmenite occurrence the amount of Ti remaining in the melt is 100%, we consider that up to 15% of the bulk Ti resides in LMO silicates at the point of ilmenite-saturation (Millet *et al.*, 2016). The closest modelled cumulate composition that is consistent with the estimate for the high-Ti source of Millet *et al.* (2016) is the Lin *et al.* (2017) cumulate (91% PCS, $\delta^{49}\text{Ti}_{\text{cumulate}} = -0.06 \text{ ‰}$; Millet *et al.* (2016) $\delta^{49}\text{Ti}_{\text{cumulate}} = -0.068 \text{ ‰}$). This IBC component, containing 5 % of ilmenite, is assimilated (AFC) by a low-Ti magma (at 20 % partial melting). With ongoing fractional crystallisation of this low-Ti basaltic magma (crystallising mineral assemblage 60 % olivine, 40 % opx + cpx), we subsequently increase the portion of assimilated IBC material to 45 %. For bulk-addition, we use the same partial melt composition as for AFC. Via a mass balance $C_{\text{tot}} = C_{\text{low-Ti}} \times X_{\text{low-Ti}} + C_{\text{IBC}}(1 - X_{\text{low-Ti}})$ an increasing amount of the IBC component ($\delta^{49}\text{Ti}_{\text{cumulate}} = -0.06 \text{ ‰}$) is added into the melt as fractional crystallisation proceeds (crystallising mineral assemblage 60 % olivine, 40 % opx + cpx). Our models (Fig. S-7a) consistently show that $\delta^{49}\text{Ti}$ and Ta/Hf of the melt converge towards the IBC compositions, as this component dominates the HFSE and Ti budget. Both AFC and bulk-addition models evolve slightly differently with regards to their source: This is because the 12004-like composition initially starts with significantly higher Ta and Hf compared to the modelled cumulate. These higher concentrations lessen the impact of IBC-assimilation onto the 12004-derived magma in both processes. In all cases, however, the mixing process imparts a negative $\delta^{49}\text{Ti}$ onto the existing melt as assimilation proceeds. This effect is smallest in the AFC-evolution line from the 12004-derived composition, as the initial Ti concentration of the melt is initially higher than for the modelled cumulate. This in turn dilutes the Ti isotope composition imparted onto the melt by the IBC component. In a third approach, we modelled the mixing between an IBC-derived partial melt and a low-Ti partial melt. Similar to 4.3, the composition of (ilmenite-bearing) Apollo 17 sample 70017 (similar to Shih *et al.*, 1975) is used as an IBC-derived partial melt. The low-Ti magma is a partial melt from the 90 % PCS Charlier *et al.* (2018) cumulate assemblage with the 12004-like composition. With an aggregate fractional melting model, a partial melt from both source compositions is modelled. These two generated melts are then mixed in three scenarios: The IBC-derived partial melt (fixed at 10%) is mixed into the low-Ti melt in a fixed mixing proportion of 0.2:0.8, while the degree of partial melting in the low-Ti melt is subsequently increased up to 35 %. In the second scenario, a partial melt from the IBC (fixed at 10 % partial melting) is mixed into a low-Ti magma (fixed at 25 % partial melting) in gradually increasing proportions. Lastly, an IBC-derived partial melt (fixed at 25 % partial melting) is mixed into a low-Ti magma (fixed at 25 % partial melting). Again, the proportion of the IBC-derived melt admixed into the low-Ti melt is subsequently increased. The concentrations of the resulting magma-mixture are calculated with a mass balance $C_{\text{tot}} = C_{\text{low-Ti}} \times X_{\text{low-Ti}} + C_{\text{IBC}}(1 - X_{\text{low-Ti}})$. Due to the absence of ilmenite in the source of the low-Ti melt, its Ti isotope composition is expected to be unfractionated relative to OL-Ti. The IBC-derived melt will have fractionated, *i.e.*, positive $\delta^{49}\text{Ti}$ due to the partial melting of an ilmenite-bearing cumulate. In the first scenario, the Ta/Hf of the low-Ti magma decreases in the mixture from ~ 0.2 to 0.15 at low degrees of partial melting, with only a small increase in $\delta^{49}\text{Ti}$. At around 6 % partial melting, the resulting melt shows an increase in both its Ta/Hf and $\delta^{49}\text{Ti}$. Finally, at 35 % partial melting, the resulting mixed melt has a Ta/Hf of ~ 0.14 and a $\delta^{49}\text{Ti}$ of $\sim +0.015$, well below the observed range for high-Ti mare basalts. However, as the proportion of IBC steadily increases, the mixture of the two partial melts (fixed at 10 %



partial melting for IBC-component and 25 % partial melting for the low-Ti component, respectively) is characterised by a steady increase of Ta/Hf_{melt} and $\delta^{49}\text{Ti}_{\text{melt}}$. In order to reach even the observed range of $\delta^{49}\text{Ti}$ and Ta/Hf in high-Ti mare basalts, the required proportion of IBC-material in the mixed melt would need 100% of IBC-derived material (essentially 0 % of the low-Ti magma), which is an unrealistic expectation. In the third scenario, we increased the degree of partial melt for the IBC-component to 25%. Again, the scenario (fixed IBC-derived partial melt 25%, fixed low-Ti derived partial melt 25%, and subsequently increasing addition of IBC-melt into the mixture) only reaches the observed range of $\delta^{49}\text{Ti}$ and Ta/Hf in high-Ti mare basalts once the partial melt is essentially exclusively derived from the IBC component. The observed range of $\delta^{49}\text{Ti}$ and Ta/Hf in our high-Ti basalts cannot be explained by mixing: The IBC component partial melting model in 4.3 shows that the observed range in $\delta^{49}\text{Ti}$ and Ta/Hf in Apollo 17 high-Ti samples is accurately reproduced after 20-30 % partial melting. The low-Ti magma is not expected to have experienced prior Ti isotope fractionation, thus the $\delta^{49}\text{Ti}_{\text{melt}}$ in this mixing model is constrained by the partial melt generated from the IBC component. Even if a melt (45-50 % partial melting) would be assimilated by a low-Ti magma, as long as it does not consist of 100% IBC-derived melt, the $\delta^{49}\text{Ti}$ of the resulting mixture would be lower (*i.e.*, diluted) by a low-Ti magma with an $\delta^{49}\text{Ti} = 0$ ‰.

4.6 Other isotope systems

Elements with similar partitioning behaviour to Ti should be affected by the same processes, *i.e.* fractional crystallisation and partial melting, respectively. The partitioning of such elements should also lead to isotope fractionation, if the coordination in melt and mineral are similar to Ti.

Vanadium: Vanadium and its isotopes behave similarly to Ti and Fe (*e.g.*, Millet *et al.*, 2016; Sossi and Moynier, 2017), and should primarily be fractionated during crystallisation or melting of ilmenite (Ringwood, 1970). Hopkins *et al.* (2019) determined V isotopes for a representative range of lunar samples. The observed V isotope variations by Hopkins *et al.* (2019) show no systematic covariation with TiO₂ or SiO₂. It is demonstrated in their study that the variation in $\delta^{(51\text{V}/50\text{V})}_{\text{AlfaAesar}}$ is directly proportional to exposure age and the Ti and Fe content in the sample. As such, after correction for neutron capture (nc) effect, V isotope compositions show no resolvable variations relative to the Earth.

Hafnium (coupled with Neodymium): Sprung *et al.* (2013) could associate heterogeneous petrogenetic sources to Apollo mare basalts after nc-correction using Hf and Nd isotope systematics. Although promising, the number of samples where ϵNd_i and ϵHf_i as well as $\delta^{49}\text{Ti}$ have been determined is too small to come to any robust conclusion regarding the effect of source heterogeneity on the Ti isotope composition.

Iron: As in the case of Ti, Fe is compatible in ilmenite and displays lower spatial coordination in silicate melts, and because of this, ilmenite-melt equilibria during melting or crystallization will lead to mass-dependent Fe isotope fractionation (Sossi and Moynier, 2017 and references therein). Poitrasson *et al.* (2004) observe a systematic shift towards heavier Fe isotope compositions in lunar samples relative to the Earth. Later studies found that the Mg Suite rocks have lower $\delta^{(57\text{Fe}/54\text{Fe})}_{\text{IRMM-014}}$ (henceforth $\delta^{57}\text{Fe}$) than low-Ti basalts, which in turn have lower $\delta^{57}\text{Fe}$ than high-Ti mare basalts (Poitrasson *et al.*, 2019; Sossi and Moynier, 2017; Weyer *et al.*, 2005). The bimodal $\delta^{57}\text{Fe}$ distribution of low-Ti and high-Ti mare basalts is attributed to whether ilmenite is involved or not during partial melting (Sossi and Moynier, 2017; Sossi and O'Neill, 2017). The higher $\delta^{57}\text{Fe}$ of high-Ti mare basalts originates from the partial melting of their ilmenite-bearing source (IBC), which is supported by previous experimental studies (*e.g.*, Shih *et al.*, 1975) and by our findings using Ta/Hf and $\delta^{49}\text{Ti}$ systematics. Observed intra-group variations of $\delta^{49}\text{Ti}$ in low-Ti ilmenite basalts, ONBs and QNBs in this study do not persist in Fe isotope compositions reported by Weyer *et al.* (2005), Sossi and Moynier (2017) or Poitrasson *et al.* (2019). The absence of a distinguishable Fe isotope signature of fractional crystallisation of ilmenite or lack thereof in low-Ti mare basalts is consistent with the uniform Fe fractionation factor for olivine and ilmenite of $\Delta^{57}\text{Fe}_{\text{ilm-ol}} = +0.01$ ‰ (Sossi and O'Neill, 2017). This uniform Fe fractionation factor imparts $\delta^{57}\text{Fe}$ of the same magnitude onto low-Ti ilmenite basalts, ONBs and QNBs. The different fractionation behavior of Ti and Fe reveal an offset in low-Ti ilmenite basalts compared to ONBs/QNBs and high-Ti mare basalts (Fig. S-9a). Consequently, a coupled $\delta^{49}\text{Ti}$ - $\delta^{57}\text{Fe}$ study may be able to investigate the petrogenetic processes of lunar sample in further detail. The number of samples where both Ti and Fe isotope compositions have been determined however is yet too little to confidently investigate the different petrogenetic trends in $\delta^{57}\text{Fe}$ *vs.* $\delta^{49}\text{Ti}$ or Ta/Hf.

Chromium: Mass-dependent isotope variations have also been reported for moderately volatile Cr (Bonnand *et al.*, 2016). Chromium in general can be compatible in pyroxene, spinel and ilmenite (Leitzke *et al.*, 2016). At lunar $f\text{O}_2$, the predominant Cr species is Cr²⁺, whereas its dominant terrestrial redox species is Cr³⁺. The difference in $\delta^{(53\text{Cr}/52\text{Cr})}_{\text{NBS-979}}$, henceforth $\delta^{53}\text{Cr}$, between Bulk Silicate Earth and Bulk Silicate Moon is attributed to mass-dependent fractionation during to evaporative loss (Sossi *et al.*, 2018). Unlike in Ti and Fe isotope systematics, fractional crystallisation of Cr-bearing minerals imparts a lighter $\delta^{53}\text{Cr}$ onto the melt. The variations of $\delta^{53}\text{Cr}$ in low-Ti and high-Ti mare basalts are consistent with fractional crystallisation of pyroxene and spinel (Apollo 12 low-Ti mare basalts) and (pyroxene,) spinel and ulvö-spinel (Apollo 11 and 17 high-Ti mare basalts; Bonnand *et al.*, 2016). If both Cr and Ti were to be affected by fractional crystallisation, a negative covariation between $\delta^{49}\text{Ti}$ and $\delta^{53}\text{Cr}$ would be expected. This is especially interesting given an observed negative covariation of $\delta^{53}\text{Cr}$ *vs.* TiO₂ in Apollo 12 low-Ti samples



analysed by Bonnand *et al.* (2016). Low-Ti ilmenite basalts should have experienced fractional crystallisation of ilmenite and ulvöspinel (supported by this study and the steady decrease in TiO₂-contents observed in Bonnand *et al.*, 2016). However, even combining data from Millet *et al.* ($\delta^{49}\text{Ti}$; 2016) Bonnand *et al.* ($\delta^{53}\text{Cr}$; 2016), Sossi *et al.* ($\delta^{53}\text{Cr}$; 2018), available data are scarce. Sample groups where both systems have been determined include two Apollo 11 samples (sample 10057 was measured by both Bonnand *et al.* (2016) and Sossi *et al.* (2018)), one Apollo 12 sample, one Apollo 14 sample, three Apollo 15 samples (sample 15555 has been determined by Bonnand *et al.* (2016), horizontal scatter) and Sossi *et al.* (2018)) and three Apollo 17 samples (negative correlation, Fig. S-9b). While promising, to the scarcity of available data prevents us to reliably investigate possible coupled mass-dependent isotope variations in $\delta^{53}\text{Cr}$ and $\delta^{49}\text{Ti}$ for these samples.

See Table S-7 for the $\delta^{49}\text{Ti}$, the main- and trace-element data used in this study.



Supplementary Tables**Table S-1** Short characterisation of the analysed lunar samples. All information by the Lunar Sample Compendium (Meyer, 2012 and references therein).

NASA ID	Mission Nr	Rock Type	TiO ₂ (wt. %)	SiO ₂ (wt. %)	Additional information
KREEP-rich samples					
14305	Apollo 14	Breccia	~1	48	Basalts clasts are like 14310.
14310	Apollo 14	KREEP basalt	1.3	48	Between 1-3 % opaque phases; Pyroxenes contain ilmenite, High Ir and Ni content.
68115	Apollo 16	Breccia	0.5	44	May consist of a bomb from South Ray Crater.
72275	Apollo 17	Breccia	1	48	May be ejecta from Serenitatis basin; Shows contamination by meteorite material.
Ilmenite basalts (High-Ti)					
10017	Apollo 11	Ilmenite Basalt	11	40	One of two lava flows (high-K); Up to 15 modal% ilmenite.
10057	Apollo 11	Ilmenite Basalt	11	40	One of two lava flows (high-K); 15 % opaque phases, probably ilmenite.
10020	Apollo 11	Ilmenite Basalt	11	40	One of two lava flows (low-K); formed from an Fe-Ti rich liquid; Composition very similar to 75016 and 75035.
75035	Apollo 17	Ilmenite Basalt	9	42	Around 15 % ilmenite; Mafic parental magma.
74275	Apollo 17	Ilmenite Basalt	13	38	Around 30 % opaque phases; High amounts of Ti ³⁺ and high amounts of armacolite.
74255	Apollo 17	Ilmenite Basalt	13	38	Around 15-20 % opaque phases and abundant ilmenite. Contains armacolite.
Ilmenite basalts (Low-Ti)					
12022	Apollo 12	Ilmenite Basalt	3	45	Around 1-9 % opaque phases.
12051	Apollo 12	Ilmenite Basalt	5	46	Around 10 % opaque phases and 5% ilmenite; ilmenite cuts through silica.
12054	Apollo 12	Ilmenite Basalt	5	44	Around 5 % ilmenite and 2 % chromite.
12063	Apollo 12	Ilmenite Basalt	5	43	Highest modal % of ilmenite among Apollo 12 samples; Shock features
Olivine-, Quartz-normative and Pigeonite basalts (Low-Ti)					
12004	Apollo 12	Olivine basalt	2.8	45	1-9 % opaque phases; Mostly Al-rich chromite overgrown with ulvö-spinel and ilmenite.
12053	Apollo 12	Pigeonite basalt	1.6	46	Around 4 % ilmenite.
15065	Apollo 15	Quartz-normative basalt	1.5	48	2 % opaque phases; May not be related to other Apollo 15 basalts.
15495	Apollo 15	Quartz-normative basalt	1.8	48	
15555	Apollo 15	Olivine-normative basalt	2.3	44	Primitive endmember of the Ol-normative Apollo 15 suite.
15556	Apollo 15	Olivine-normative basalt	2.7	46.2	Around 2 % ilmenite, very vesicular.
15545	Apollo 15	Olivine-normative basalt	2.4	45	Around 3.4 % ilmenite.
15058	Apollo 15	Quartz-normative basalt	1.8	48	Exsolution features suggest slow cooling.



Table S-2 Isotope composition of our double spike and our in-house reference material, OL-Ti data from Millet *et al.* (2014) for reference.

	$^{46}\text{Ti}/^{47}\text{Ti}$	$^{48}\text{Ti}/^{47}\text{Ti}$	$^{49}\text{Ti}/^{47}\text{Ti}$
OL-Ti	1.092874	10.070565	0.749766
2se	0.000011	0.000086	-
Millet <i>et al.</i> (2016) - Double spike	0.032663	0.270783	0.945969
2se	0.000001	0.000007	0.000013
Cologne double spike	0.006224	0.07996	1.072000
2se	0.000018	0.00015	0.000065
Cologne Col-Ti Ref.-mat	1.092759	10.071601	0.749919
2se	0.000002	0.000019	0.000003
[c] DS, Ti_{tot}	410.9 ± 0.3 µg/g		



Table S-3 Results of reference materials with varying sample to spike ratios. Each sample was measured three times and bracketed by ideally spiked Col-Ti and OL-Ti for additional quality control.

Reference Material	f_{sample}	$^{48}\text{Ti}/^{47}\text{Ti}_{\text{mix,measured}}$	2 s.d.	$\delta(^{49}\text{Ti}/^{47}\text{Ti})_{\text{OL-Ti}}$	2 s.d.	n	95 % c.i.
Col-Ti	0.90	6.2661	0.0011	-0.152	0.067	3	0.083
Col-Ti	0.80	4.16766	0.00022	0.109	0.050	3	0.063
Col-Ti	0.70	2.94295	0.00011	0.197	0.031	3	0.038
Col-Ti	0.65	2.52532	0.00021	0.199	0.013	3	0.016
Col-Ti	0.60	2.20163	0.00013	0.1940	0.0090	3	0.011
Col-Ti	0.55	1.78385	0.00011	0.2182	0.0043	3	0.0053
Col-Ti	0.51	1.6142	0.0078	0.218	0.017	3	0.022
Col-Ti	0.45	1.293016	0.000049	0.2150	0.0090	3	0.011
Col-Ti	0.40	1.097546	0.000034	0.195	0.010	3	0.012
Col-Ti	0.35	0.881946	0.000011	0.1700	0.0090	3	0.011
Col-Ti	0.30	0.751503	0.000064	0.138	0.010	3	0.013
Col-Ti	0.20	0.480887	0.000010	0.018	0.010	3	0.012
OL-Ti	0.80	3.57164	0.00039	-0.0339	0.0031	3	0.0038
OL-Ti	0.55	1.483742	0.000094	0.029	0.022	3	0.027
OL-Ti	0.51	1.284446	0.000024	0.012	0.010	3	0.012
OL-Ti	0.45	1.049865	0.000037	0.001	0.022	3	0.027
OL-Ti	0.20	0.397393	0.000027	-0.276	0.039	3	0.049
BCR-2	0.89	5.9691	0.0015	-0.38	0.12	3	0.15
BCR-2	0.79	4.14241	0.00020	-0.124	0.011	3	0.014
BCR-2	0.68	2.87956	0.00019	-0.029	0.041	3	0.050
BCR-2	0.52	1.76271	0.00002	0.020	0.060	3	0.074
BCR-2	0.49	1.5354	0.0000	0.018	0.025	3	0.031
BCR-2	0.43	1.258582	0.000033	0.009	0.019	3	0.023
BCR-2	0.28	0.729415	0.000081	-0.070	0.061	3	0.076
BCR-2	0.18	0.401413	0.000149	-0.160	0.072	3	0.089
Session averages							
Session I							
Col-Ti				0.199	0.039	28	0.008
OL-Ti				0.000	0.018	8	0.008
Session II							
Col-Ti				0.193	0.047	26	0.010
OL-Ti				0.000	0.012	8	0.005
BCR-2 ideal range				0.005	0.045	4	0.017
Total averages							
Col-Ti				0.196	0.043	54	0.006
OL-Ti				0.000	0.015	16	0.004



Table S-4 Amount of Ca, $^{44}\text{Ca}/^{47}\text{Ti}$ and resulting $\delta^{49}\text{Ti}$ of Ca-doped Col-Ti solutions.

ng/ μL Ca	$^{44}\text{Ca}/^{47}\text{Ti}_{\text{measured}}$	2 s.d.	$\delta(^{49}\text{Ti}/^{47}\text{Ti})_{\text{OL-Ti}}$	2 s.d.	n	95 % c.i.
1	0.0004325	0.0000047	0.219	0.057	3	0.071
10	0.0011534	0.0000010	0.243	0.038	3	0.047
100	0.010093	0.000025	0.265	0.044	3	0.054
500	0.049157	0.000058	0.437	0.023	3	0.029
1000	0.098285	0.000099	0.616	0.030	3	0.037

Table S-5 Used mineral assemblages for the modelling.

Used mineral assemblages							
Xs	Ol	Opx	Cpx	Plg	Pig	Ilm	
<i>Snyder et al. (1992)</i>							
10	1						
40		1					
76	0.25			0.53	0.22		
95			0.24	0.32	0.34	0.11	
<i>Lin et al. (2017)</i>							
10	0.83	0.15	0.02				
50	0.36	0.54	0.096				
63.8	0.59	0.34	0.074				
68.5	0.11	0.41	0.138	0.34			
76.1	0.1	0.46	0.144	0.3			
79.3	0.1	0.23	0.072	0.6			
82.8		0.32	0.101	0.58			
87.2		0.35	0.15	0.5			
91.1		0.32	0.235	0.45			0.05
96.4		0.16	0.168	0.39			0.12
<i>Charlier et al. (2018)</i>							
10	1						
51.1	0.9	0.1					
78.1	0.05	0.2		0.5	0.25		
81.1			0.2	0.48	0.32		
97.1	0.2		0.16	0.42			0.12
<i>Rapp et al. (2018)</i>							
10	1						
52.3		1					
74.6	0.27	0.06	0.31	0.36			
89.5			0.54	0.46			
97.3			0.5	0.45			0.045
97.8	0.091		0.409	0.27	0.045	0.091	



Table S-6 Partition coefficients used in the fractional crystallisation and Rayleigh model.

Mineral phase	Conditions				Partition coefficients					Reference
	Ti in melt	fO ₂	T (°C)	Proportion of Ti ³⁺	Ti			Ta	Hf	
					Ti ³⁺	Ti ⁴⁺	Ti _{tot}			
Olivine	10 % Ti	IW - 1.6	1280	0		0.0088	0.0088	0.000040	0.00021	Leitzke <i>et al.</i> (2016)
Clinopyroxene	10 % Ti	IW - 1.6	1250	0		0.19	0.19	0.00084	0.020	Leitzke <i>et al.</i> (2016)
Orthopyroxene	20 % Ti	IW - 1.6	1250	0		0.12	0.12	0.00042	0.0043	Leitzke <i>et al.</i> (2016)
Ilmenite	10 % Ti	IW - 1.8	1100	0		4.7	4.7	1.7	0.76	Leitzke <i>et al.</i> (2016)
Plagioclase	10 % Ti	FMQ - 0.1	1230	0		0.022	0.022	0.053	0.00014	Leitzke <i>et al.</i> (2016)
Pigeonite						0.071	0.071	0.0047	0.022	van Westrenen <i>et al.</i> (2000)
Ol				30 %	0.044	0.0042	0.016			Mallmann and O'Neill (2009)
Opx				30 %	0.033	0.095	0.077			Mallmann and O'Neill (2009)
Cpx				30 %	1.1	0.029	0.35			Mallmann and O'Neill (2009)



Table S-7 Detailed trace element data for our analysed samples. bce = breccia, ilm = ilmenite; QNB = quartz-normative basalt, ONB = olivine-normative basalt, olv = olivine, pgt = pigeonite.

Data - This study			Ti isotope data				Quality Control			
NASA ID	Mission	Rock type	$\delta^{49}\text{Ti}$	2 s.d.	N	95 % c.i.	Interference monitor		Spike:Sample proportion	
							$^{44}\text{Ca}/^{47}\text{Ti}_{\text{measured}}$	2 s.d.	$^{48}\text{Ti}/^{47}\text{Ti}_{\text{mix,measured}}$	2 s.d.
10017	Apollo 11	High-Ti ilm basalt	0.009	0.024	6	0.012	1.87E-04	1.13E-06	1.95368	0.00025
10020		High-Ti ilm basalt	0.011	0.022	6	0.011	5.57E-05	1.04E-06	1.88218	0.00015
10057		High-Ti ilm basalt	0.009	0.024	6	0.012	1.11E-04	1.27E-06	2.01535	0.00010
74255	Apollo 17	High-Ti ilm basalt	0.043	0.010	6	0.005	5.24E-05	5.01E-07	1.889048	0.000059
74275		High-Ti ilm basalt	0.045	0.010	6	0.005	2.52E-05	4.13E-07	1.92915	0.00014
75035		High-Ti ilm basalt	0.115	0.025	6	0.013	2.38E-05	7.20E-07	1.942528	0.000086
79135	Apollo 17	High-Ti Bce	0.019	0.017	6	0.009	3.13E-04	1.05E-06	2.152307	0.000072
79035		High-Ti Bce	0.047	0.018	6	0.010	6.96E-05	1.38E-06	1.89691	0.00017
14305	Apollo 14	KREEP-rich Bce	0.296	0.030	6	0.016	9.22E-05	1.96E-06	1.74719	0.00021
68115	Apollo 16	KREEP-rich Bce	0.117	0.027	6	0.014	4.20E-04	3.76E-06	3.73312	0.00047
72275	Apollo 17	KREEP-rich Bce	0.185	0.026	6	0.014	1.26E-04	6.62E-06	2.31779	0.00015
14310	Apollo 14	KREEP basalt	0.263	0.035	6	0.018	9.83E-05	3.78E-06	2.03541	0.00024
15058	Apollo 15	Low-Ti QNB	-0.010	0.034	6	0.018	1.10E-04	1.53E-06	2.72418	0.00014
15065		Low-Ti QNB	-0.030	0.014	6	0.007	3.46E-04	2.00E-06	2.82205	0.00013
15495		Low-Ti QNB	0.011	0.017	6	0.009	3.14E-04	5.19E-07	2.28619	0.00020
15545		Low-Ti ONB	0.011	0.032	6	0.017	3.06E-04	9.72E-07	1.98179	0.00012
15556		Low-Ti ONB	0.007	0.030	6	0.016	1.08E-04	1.95E-06	2.02256	0.00011
15555		Low-Ti ONB	-0.008	0.026	6	0.014	1.06E-03	6.62E-07	2.216530	0.000095
12022	Apollo 12	Low-Ti ilm basalt	0.029	0.022	6	0.011	1.15E-03	1.18E-06	1.89341	0.00014
12051		Low-Ti ilm basalt	0.030	0.022	8	0.009	2.14E-04	1.03E-06	1.939443	0.000086
12063		Low-Ti ilm basalt	0.055	0.022	6	0.012	5.53E-04	1.95E-06	1.87343	0.00022
12054		Low-Ti ilm basalt	0.028	0.026	6	0.014	5.38E-04	8.80E-07	2.10094	0.00028
12004	Apollo 12	Low-Ti olv basalt	0.006	0.010	6	0.005	2.41E-04	1.34E-06	2.09198	0.00030
12053	Apollo 12	Low-Ti pgt basalt	-0.013	0.026	6	0.014	4.12E-04	2.01E-06	2.00464	0.00022



Table S-7 continued Main element data are from the lunar sample compendium, HFSE data is by Thiemens *et al* (2019). bce = breccia, ilm = ilmenite; QNB = quartz-normative basalt, ONB = olivine-normative basalt, olv = olivine, pgt = pigeonite.

NASA ID	Main elements - Meyer (2012)				HFSE - Thiemens <i>et al.</i> (2019)						
	wt. %				µg/g						
	SiO ₂	TiO ₂	FeO	MgO	W	Th	U	Hf	Zr	Nb	Ta
10017	41.3	11.9	19.6	7.76	0.382	3.40	0.858	16.3	491	30.4	1.82
10020	40.7	10.6	18.5	8.06	0.331	0.667	0.180	7.31	201	17.5	1.10
10057	41.6	11.4	19.1	7.02	0.386	3.56	0.856	16.2	490	30.7	1.81
74255	38.4	12.2	18.0	10.7	0.0636	0.450	0.132	8.21	221	25.9	1.43
74275	38.7	12.7	18.0	10.2	0.0590	0.466	0.138	8.67	233	28.6	1.50
75035	42.6	10.1	18.8	6.25	0.0906	0.546	0.163	11.6	322	32.9	1.93
79135	42.3	5.15	14.8	10.4	0.189	1.34	0.368	5.88	190	15.0	0.901
79035	41.7	6.58	15.6	9.91	0.165	1.16	0.315	5.88	182	15.8	0.961
14305	48.4	1.71	10.6	10.3	1.28	16.4	4.33	28.3	1163	73.6	3.26
68115	44.8	0.34	4.00	5.79	0.549	4.45	1.17	8.92	360	23.8	0.974
72275	48.0	0.91	11.9	10.0	0.924	5.84	1.51	15.9	658	31.0	1.40
14310	48.3	1.24	7.93	8.00	1.21	10.9	2.98	20.1	817	51.4	2.31
15058	47.8	1.77	20.0	9.01	0.0592	0.576	0.150	2.76	98	6.62	0.366
15065	47.2	1.33	19.2	10.7	0.0895	0.863	0.216	3.96	139	9.96	0.522
15495	48.0	1.52	20.7	10.4	0.0692	0.670	0.169	3.07	110	6.80	0.380
15545	45.0	2.33	22.2	10.5	0.0810	0.491	0.132	2.53	85	6.15	0.374
15556	45.7	2.76	21.9	8.67	0.0882	0.512	0.154	2.67	89	6.38	0.392
15555	44.2	2.10	22.4	11.2	0.0633	0.432	0.112	2.09	70	5.01	0.304
12022	43.2	5.10	22.0	10.4	0.0881	0.677	0.182	4.29	121	6.68	0.359
12051	45.1	4.62	20.2	7.21	0.127	0.804	0.208	4.04	121	7.67	0.427
12063	43.5	5.00	21.3	9.56	0.0850	0.661	0.172	4.10	115	6.62	0.376
12054	43.3	4.63	19.6	9.22	0.123	0.977	0.2552	5.3047	153	8.91	0.499
12004	45.2	2.88	21.5	12.5	0.115	0.959	0.2599	3.4882	114	7.78	0.406
12053	47.3	3.32	19.8	8.06	0.122	1.04	0.2718	3.7636	122	8.50	0.446



Supplementary Figures

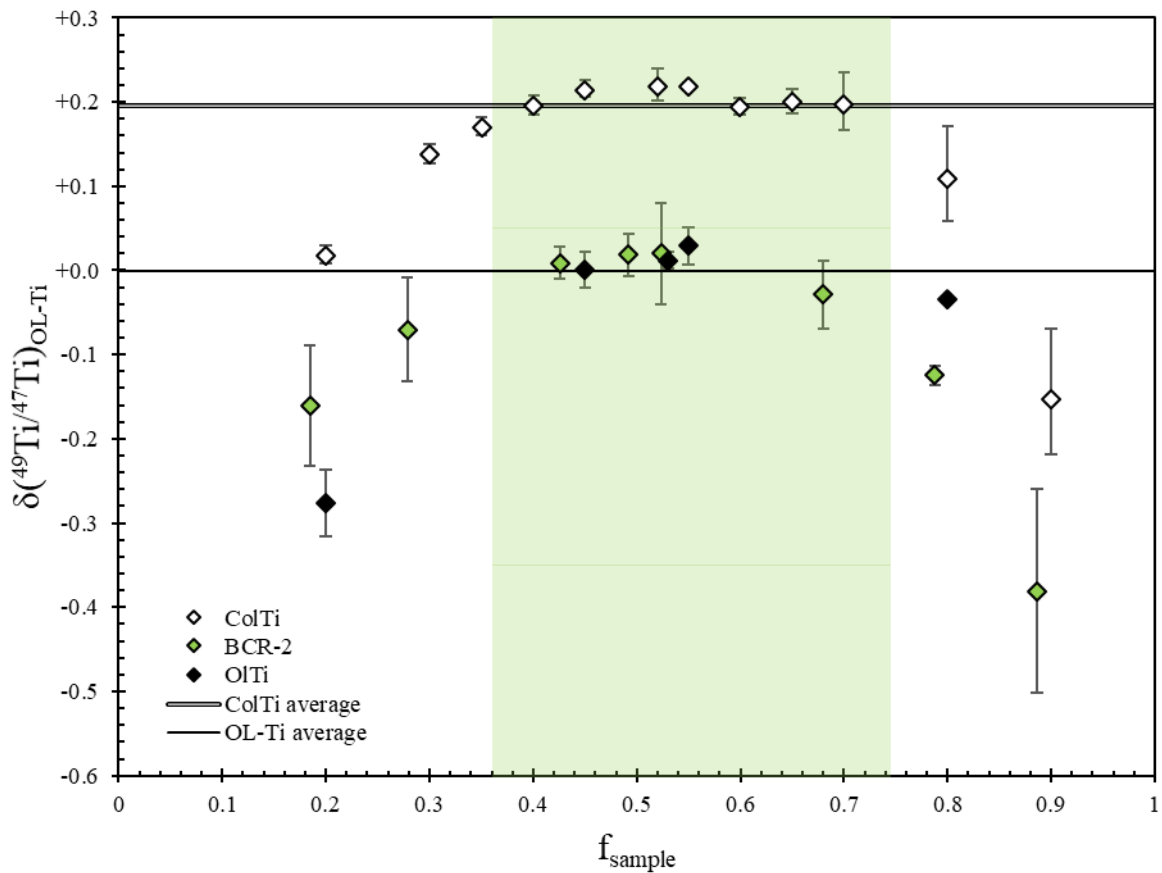


Figure S-1 $\delta(^{49}\text{Ti}/^{47}\text{Ti})_{\text{OL-Ti}}$ versus f_{sample} . The diagram illustrates the range in which the weight fraction of sample (f) in the mixture (*i.e.*, in the sample:spike proportion) reproduces published values. The green field represents the range in which spiked samples reproduce the published values. BCR-2 range average is $\delta(^{49}\text{Ti}/^{47}\text{Ti})_{\text{OL-Ti}} = +0.005 \pm 0.017 \text{ ‰}$ ($n = 12$ values of four samples with three measurements each). Precise and accurate results are obtained for sample fractions between 0.36 and 0.74 (f_{sample}). Millet *et al.* (2016) give their BCR-2 at $\delta(^{49}\text{Ti}/^{47}\text{Ti})_{\text{OL-Ti}} = -0.015 \pm 0.005 \text{ ‰}$ 95 % c.i. which overlaps with our results.

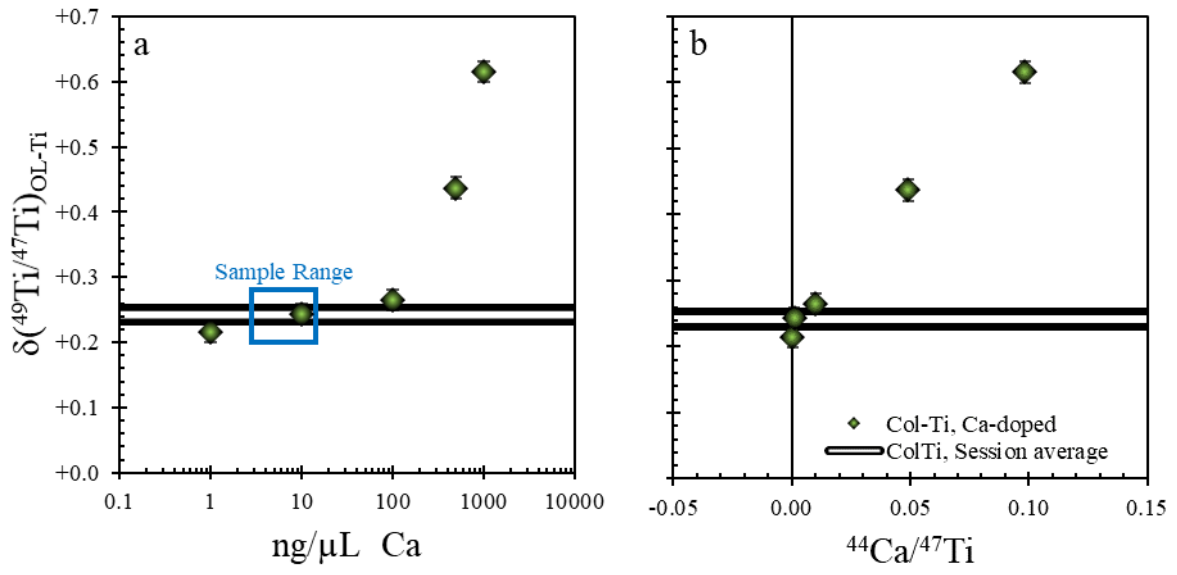
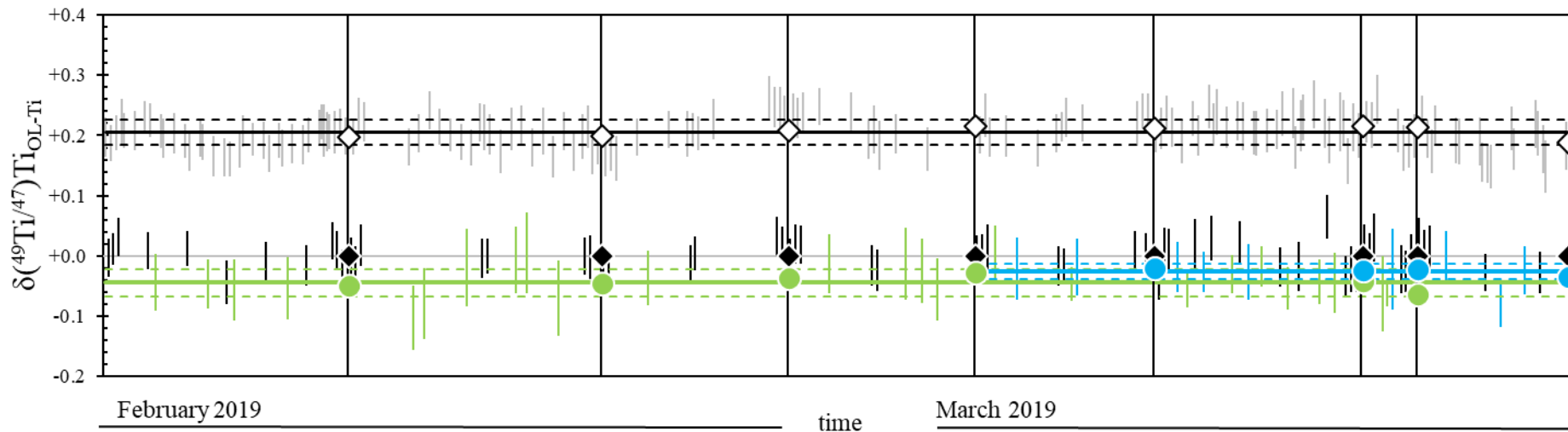


Figure S-2 Determined $\delta^{49}\text{Ti}$ Ca-doped $1\mu\text{g}/\text{mL}$ Ti Col-Ti solutions versus (a) Ca concentration and (b) $^{44}\text{Ca}/^{47}\text{Ti}$ ratio. Samples reproduce accurately up until Ca concentrations of $100\text{ ng}/\mu\text{L}$ or 100 ppb Ca . The blue box labelled "sample range" determines the measured $^{44}\text{Ca}/^{47}\text{Ti}$ -range of the analysed lunar samples. See also Table S-7.



$\delta^{49}\text{Ti}_{\text{JB-2}}$ (average)
 = -0.042 ± 0.052 ‰ (2 s.d. individual measurements, $n = 15$)
 = -0.041 ± 0.029 ‰ (2 s.d. session mean values, $n = 7$)
 = -0.043 ± 0.014 ‰ (95% c.i., $n = 7$)
 $\delta^{49}\text{Ti}_{\text{BCR-2}}$ (average)
 = -0.027 ± 0.043 ‰ (2 s.d. individual measurements, $n = 9$)
 = -0.025 ± 0.012 ‰ (2 s.d. session mean values, $n = 4$)
 = -0.025 ± 0.010 ‰ (95% c.i., $n = 4$)

◆ Sequence average OL-Ti ◇ Sequence average Col-Ti
 ● Sequence average JB-2 ● Sequence average BCR-2

$\delta^{49}\text{Ti}_{\text{Col-Ti}}$ (average)
 = 0.204 ± 0.048 ‰ (2 s.d. individual measurements, $n = 157$)
 = 0.206 ± 0.021 ‰ (2 s.d. session mean values, $n = 8$)
 = 0.206 ± 0.009 ‰ (95% c.i., $n = 8$)

Figure S-3 Reproducibility of all reference materials. Terrestrial reference materials JB-2 and BCR-2 are identical to previous studies. Each sequence was measured over the course of 24h. Sequence 7 was a shortened sequence to re-measure a sample.



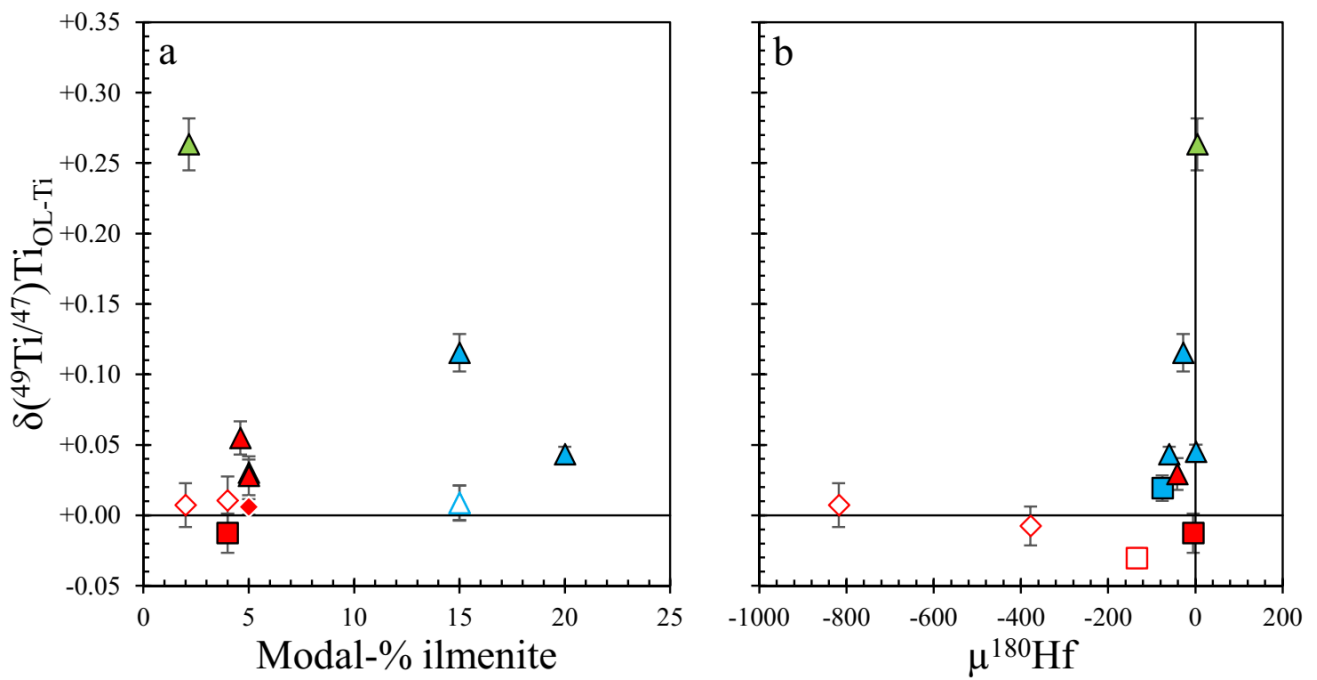


Figure S-4 (a) Modal-% ilmenite vs. $\delta^{49}\text{Ti}$ plot shows no correlation of ilmenite content with $\delta^{49}\text{Ti}$. Symbols are the same as in Figure 1 in the manuscript. **(b)** Previous studies conclude secondary neutron capture effects to be negligible in Ti DS studies (Greber *et al.*, 2017b; Mandl *et al.*, 2018). Indeed, known proxy $\mu^{180}\text{Hf}$ shows no correlation with $\delta^{49}\text{Ti}$ (Data by Sprung *et al.*, 2013); Y-axis are identical in a and b.

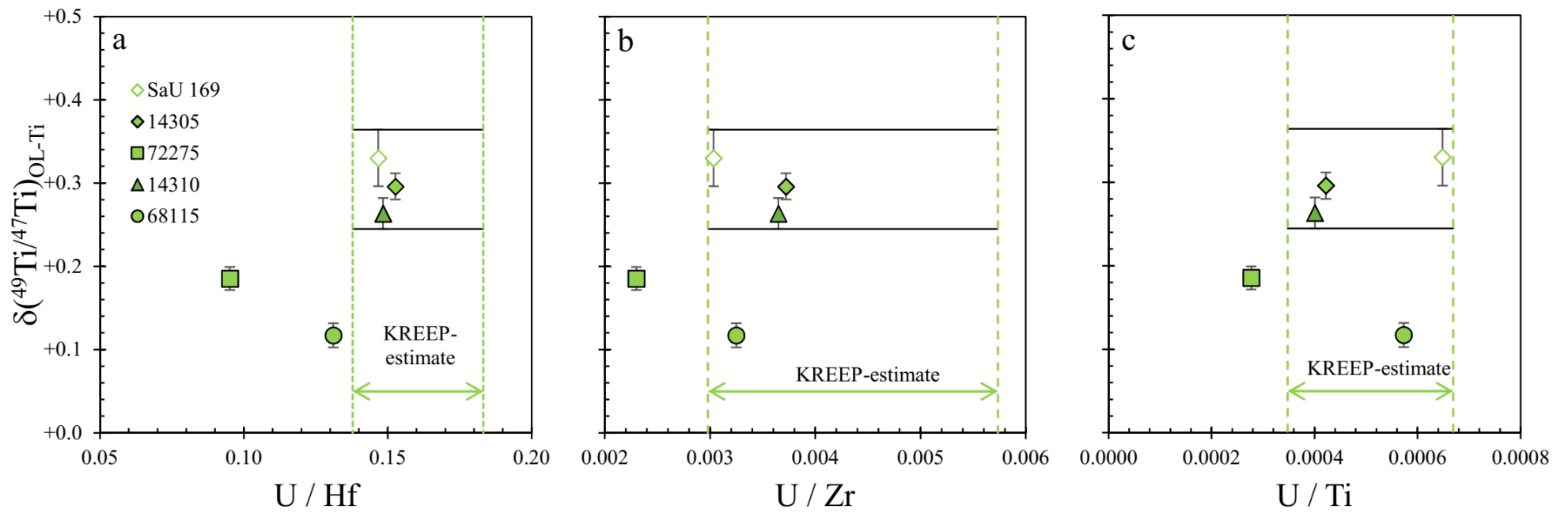


Figure S-5 Estimating the $\delta^{49}\text{Ti}$ of KREEP based on HFSE or HFSE/element ratios for (a) U/Hf, (b) – U/Zr and (c) – U/Ti. Y-axes are identical for a, b and c. KREEP-range constrained by estimates of Warren and Taylor (2014).



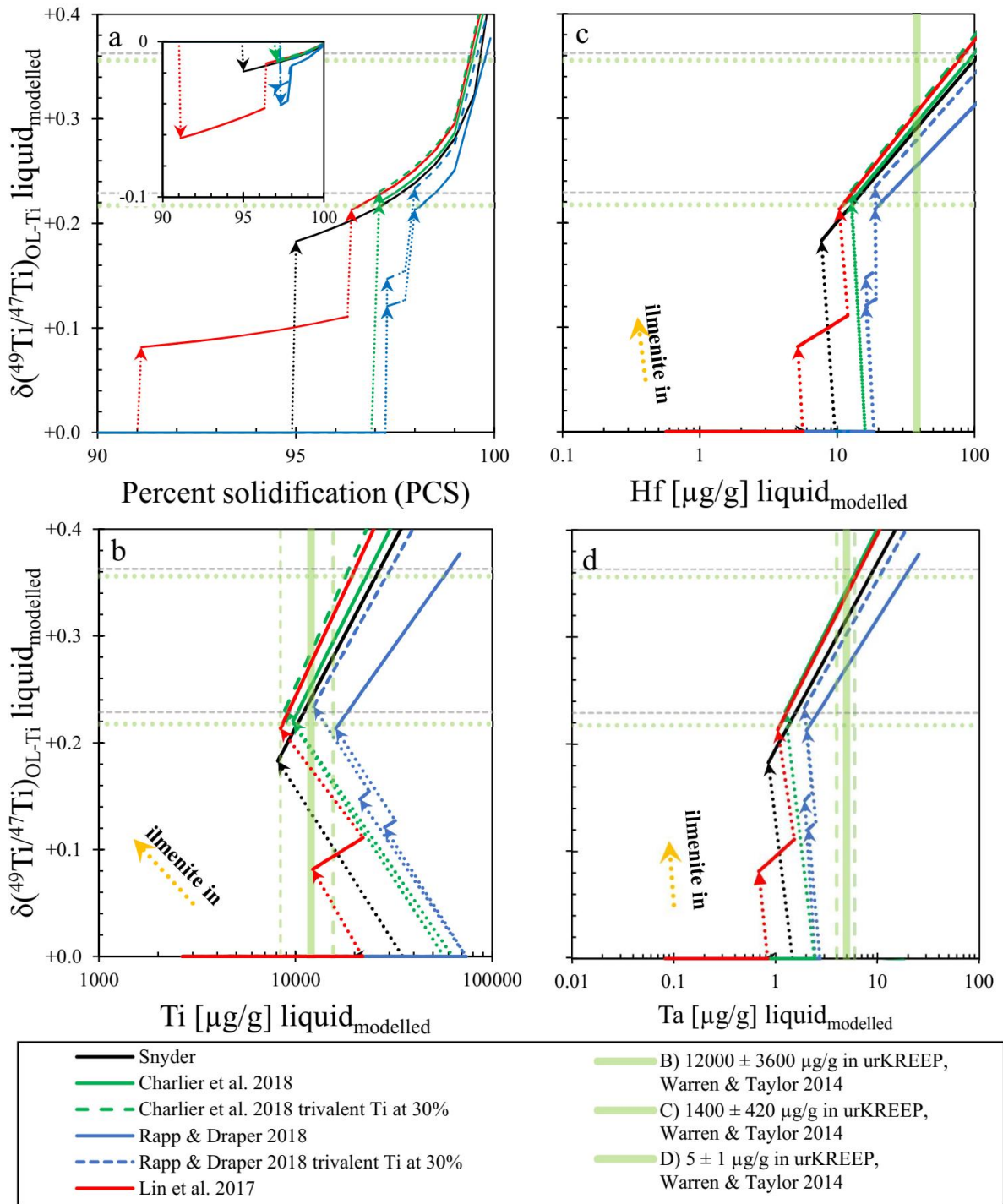


Figure S-6 All diagrams have identical y-axes and scale. **(a)** Modelled $\delta^{49}\text{Ti}$ as a function of percent solidification, the inset contains the modelled cumulates. **(b)** Modelled Ti concentration in the remaining liquid and $\delta^{49}\text{Ti}$ of the liquid. **(c)** Modelled Hf and **(d)** modelled Zr concentrations in the residual liquid, *i.e.*, urKREEP. Dotted arrows mark the point at which ilmenite is part of the mineral assemblage. Green vertical fields give the estimate of the given element by Warren and Taylor (2014), dashed vertical green lines mark the upper and lower limits of the estimates. For Hf, the limit is smaller than the size of the green bar. Horizontal green and grey lines mark the $\delta^{49}\text{Ti}_{\text{urKREEP}}$ estimate the average intersects evolution of the respective element and using U/Hf, U/Ti and U/Zr, respectively.



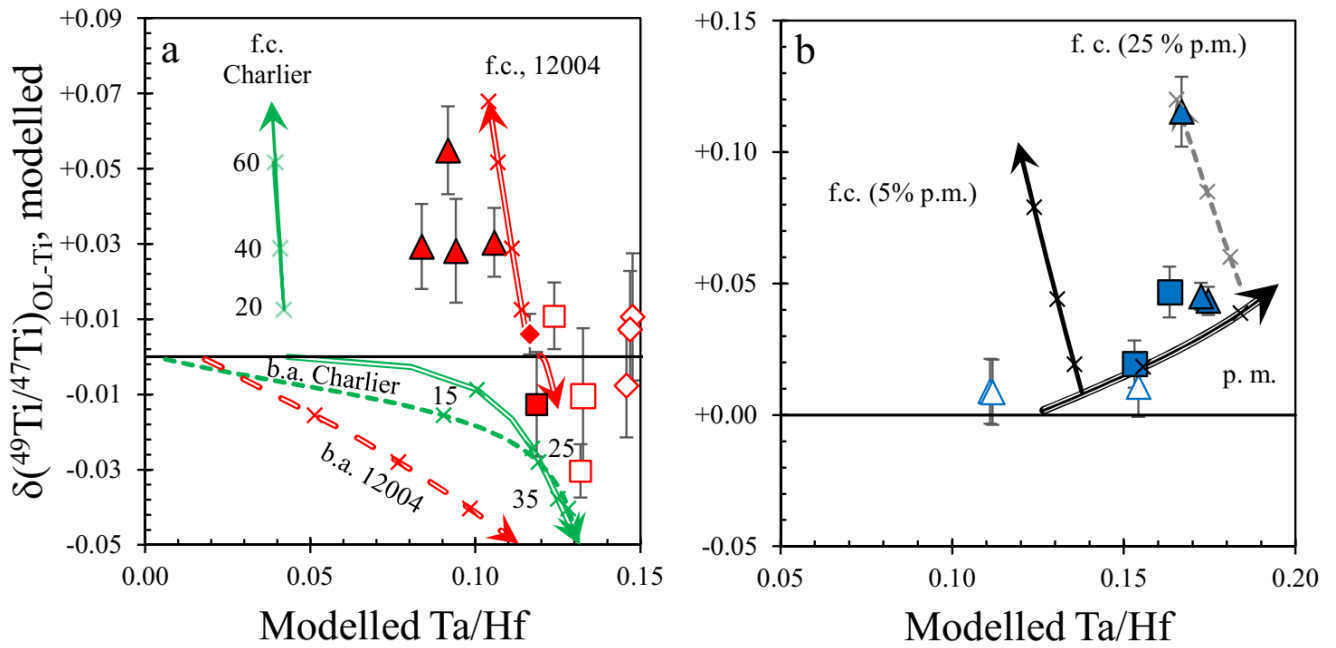


Figure S-7 (a) Modelled evolution lines for $\delta^{49}\text{Ti}$ vs. Ta/Hf for low-Ti samples and **(b)** high-Ti samples. Crosses mark 20 % steps in the fractional crystallisation, 10 % steps in the AFC/bulk addition model (15, 25 and 35 % of fractional crystallisation) and 10 % steps in partial melting model. **(a)** Solid green and red lines above $\delta^{49}\text{Ti} = 0$ ‰ display the trends of fractional crystallisation of ilmenite (f.c.) for the respective source compositions. Fractional crystallisation of ilmenite (green arrow, “f.c., Charlier”) from a partial melt from an ilmenite-free Charlier *et al.* (2018) cumulate results in a Ta/Hf well below the observed range. Green and red dashed arrow show bulk addition (b.a.) trend for the two different melt compositions of Charlier *et al.* (2018) (green) 12004 (red). The hollow green and red lines in the negative $\delta^{49}\text{Ti}$ range display the trend for AFC for the same respective sources. High-Ti sample are displayed in **(b)** and are mostly reproduced by partial melting of an IBC (p.m., black, hollow arrow), fractional crystallisation from this source cannot reproduce observed values (f.c., 5% p.m. black solid arrow) at lower degrees of partial melting. Combining partial melting and fractional crystallisation would (f.c., 25 % p.m., grey, dashed arrow) would require 35 % partial melting and concurrent fractional crystallisation of up to 60 % to reach observed $\delta^{49}\text{Ti}$ and Ta/Hf of 75035.



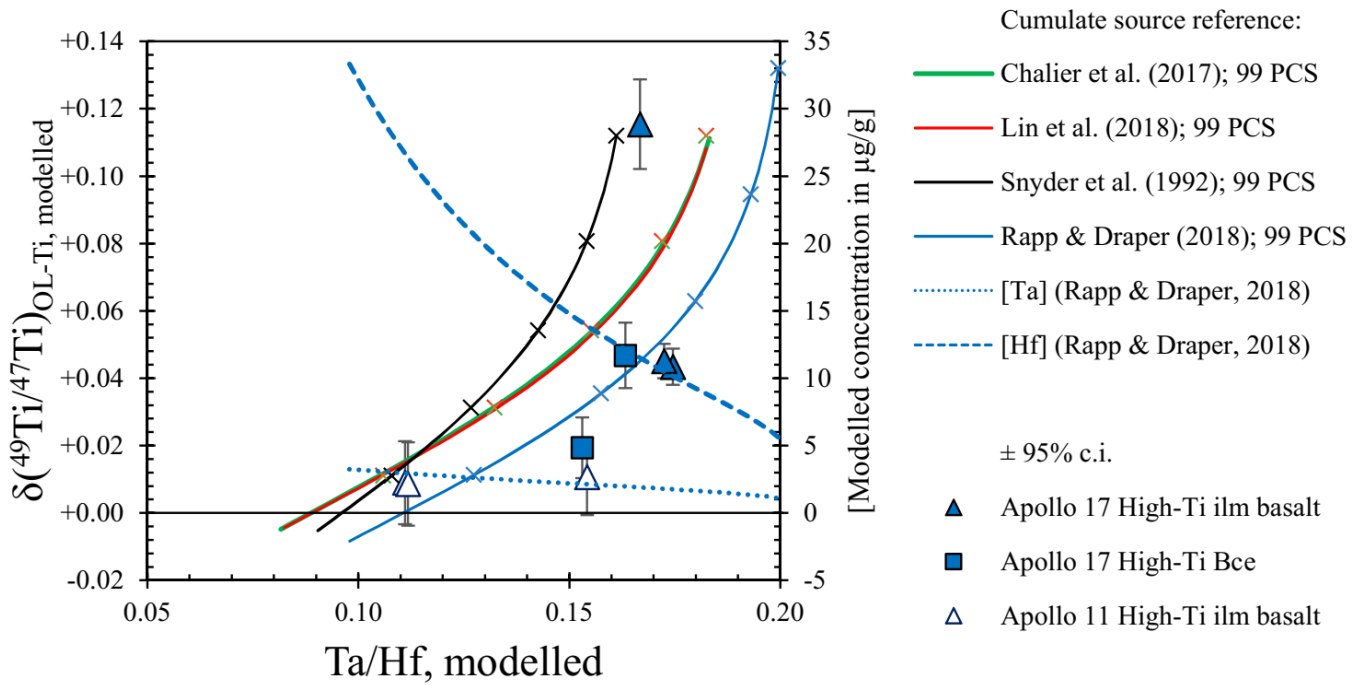


Figure S-8 Modelled Ti isotope composition versus the corresponding Ta/Hf during partial melting of an ilmenite-bearing cumulate. IBC composition corresponds to the respective model. Each cross mark represents a 10 % increase in partial melting degree. Dashed and dotted line are the modelled Hf and Ta concentration in the melt for the Rapp and Draper (2018) model.



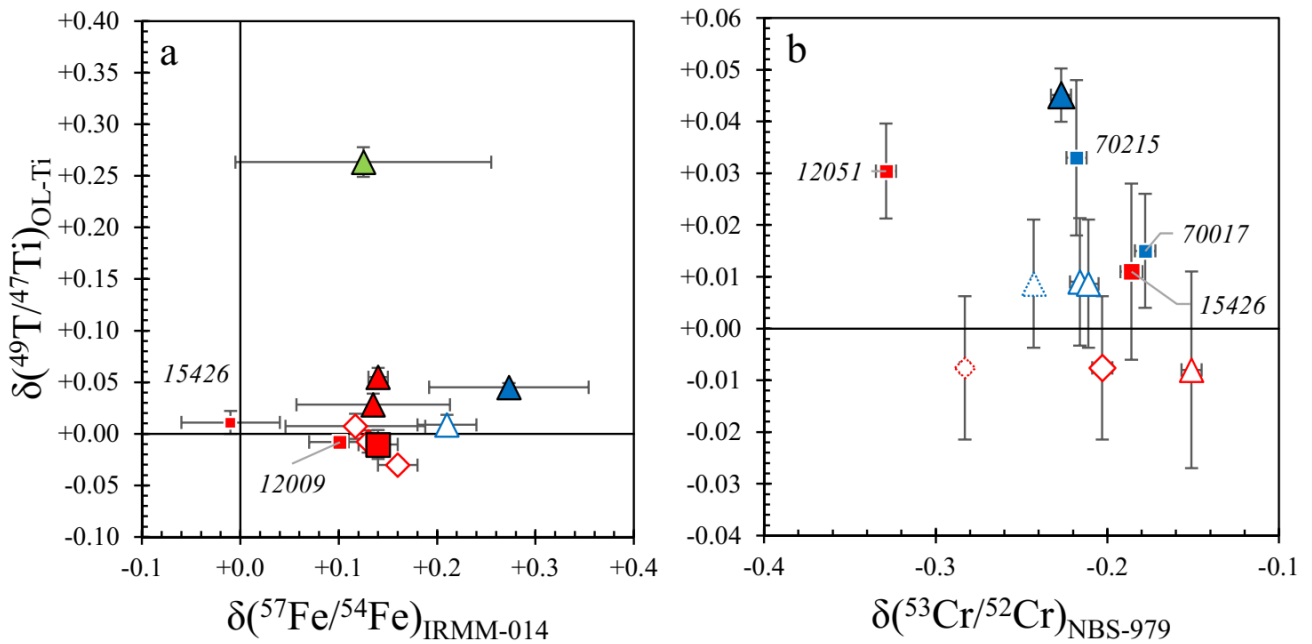


Figure S-9 (a) Coupled Fe and Ti isotope compositions of lunar samples. Additional Fe and Ti isotope data provided by previous studies basalts (Titanium data: Millet *et al.*, 2016; Iron data: Poitrasson *et al.*, 2019; Sossi and Moynier, 2017; Weyer *et al.*, 2005). **(b)** Coupled Cr and Ti isotope compositions of lunar samples. Data for 12009, 12051, 15426, 70017 and 70215 is compiled from studies by Millet *et al.* (2016), Bonnand *et al.* (2016) and Sossi *et al.* (2018). Dotted symbols in (b) are samples where two Cr isotope compositions have been determined (samples 10057 and 15555). Uncertainties for Fe and Cr are (recalculated) 2 s.e., uncertainties for Ti are 95 % c.i..

Supplementary Information References

- Bast, R., Scherer, E.E., Sprung, P., Fischer-Gödde, M., Stracke, A., Mezger, K. (2015) A rapid and efficient ion-exchange chromatography for Lu–Hf, Sm–Nd, and Rb–Sr geochronology and the routine isotope analysis of sub-ng amounts of Hf by MC-ICP-MS. *Journal of Analytical Atomic Spectrometry* 30, 2323–2333.
- Binder, A.B. (1985) The depths of the Mare basalt source region. *Journal of Geophysical Research* 90, C396.
- Bonnand, P., Parkinson, I.J., Anand, M. (2016) Mass dependent fractionation of stable chromium isotopes in mare basalts: Implications for the formation and the differentiation of the Moon. *Geochimica et Cosmochimica Acta* 175, 208–221.
- Charlier, B., Grove, T.L., Namur, O., Holtz, F. (2018) Crystallization of the lunar magma ocean and the primordial mantle-crust differentiation of the Moon. *Geochimica et Cosmochimica Acta* 234, 50–69.
- Compston, W., Oversby, V.M. (1969) Lead isotopic analysis using a double spike. *Journal of Geophysical Research* 74, 4338–4348.
- Delano, J.W., Lindsley, D.H. (1982) Chromium, Nickel, and Titanium Abundances in 74275 Olivines: More Evidence for a High-Pressure Origin of High-Titanium Mare Basalts. Thirteenth Lunar and Planetary Science Conference 1982. Lunar and Planetary Institute, Houston, Abstract #1083.
- Deng, Z., Moynier, F., Sossi, P.A., Chaussidon, M. (2018) Bridging the depleted MORB mantle and the continental crust using titanium isotopes. *Geochemical Perspectives Letters* 9, 11–15.
- Deng, Z., Chaussidon, M., Savage, P., Robert, F., Pik, R., Moynier, F. (2019) Titanium isotopes as a tracer for the plume or island arc affinity of felsic rocks. *Proceedings of the National Academy of Sciences* 201809164.
- DePaolo, D.J. (1981) Trace element and isotopic effects of combined wallrock assimilation and fractional crystallization. *Earth and Planetary Science Letters* 53, 189–202.
- Elkins-Tanton, L.T., Burgess, S., Yin, Q.-Z. (2011) The lunar magma ocean: Reconciling the solidification process with lunar petrology and geochronology. *Earth and Planetary Science Letters* 304, 326–336.
- Gerber, S., Burkhardt, C., Budde, G., Metzler, K., Kleine, T. (2017) Mixing and Transport of Dust in the Early Solar Nebula as Inferred from Titanium Isotope Variations among Chondrules. *The Astrophysical Journal* 841, L17.
- Gnos, E. (2004) Pinpointing the Source of a Lunar Meteorite: Implications for the Evolution of the Moon. *Science* 305, 657–659.
- Greber, N.D., Dauphas, N., Bekker, A., Ptáček, M.P., Bindeman, I.N., Hofmann, A. (2017a) Titanium isotopic evidence for felsic crust and plate tectonics 3.5 billion years ago. *Science* 357, 1271–1274.
- Greber, N.D., Dauphas, N., Puchtel, I.S., Hofmann, B.A., Arndt, N.T. (2017b) Titanium stable isotopic variations in chondrites, achondrites and lunar rocks. *Geochimica et Cosmochimica Acta* 213, 534–552.
- Green, D.H., Ringwood, A.E., Ware, N.G., Hibberson, W.O., Major, A., Kiss, E. (1971) Experimental petrology and petrogenesis of Apollo 12 basalts. *Lunar and Planetary Science Conference Proceedings* 2, 601.
- Green, D.H., Ringwood, A.E., Hibberson, W.O., Ware, N.G. (1975) Experimental petrology of Apollo 17 mare basalts. *Lunar and Planetary Science Conference Proceedings* 1, 871–893.
- Gross, J., Joy, K.H. (2016) Evolution, Lunar: From Magma Ocean to Crust Formation. In: Cudnik, B. (ed.) *Encyclopedia of Lunar Science*. Springer International Publishing, Cham, 1–20.
- Hopkins, S.S., Prytulak, J., Barling, J., Russell, S.S., Coles, B.J., Halliday, A.N. (2019) The vanadium isotopic composition of lunar basalts. *Earth and Planetary Science Letters* 511, 12–24.
- Johnson, A.C., Aarons, S.M., Dauphas, N., Nie, N.X., Zeng, H., Helz, R.T., Romaniello, S.J., Anbar, A.D. (2019) Titanium isotopic fractionation in Kilauea Iki lava lake driven by oxide crystallization. *Geochimica et Cosmochimica Acta* 264, 180–190.
- Kesson, S.E. (1975) Melting Experiments on Synthetic Mare Basalts and Their Petrogenetic Implications. Sixth Lunar Science Conference 1975. Lunar and Planetary Institute, Houston, Abstract #1168.
- Kesson, S.E., Ringwood, A.E. (1976) Mare basalt petrogenesis in a dynamic moon. *Earth and Planetary Science Letters* 30, 155–163.
- Kurzweil, F., Münker, C., Tusch, J., Schoenberg, R. (2018) Accurate stable tungsten isotope measurements of natural samples using a 180 W- 183 W double-spike. *Chemical Geology* 476, 407–417.
- Leitzke, F.P., Fonseca, R.O.C., Michely, L.T., Sprung, P., Münker, C., Heuser, A., Blanchard, H. (2016) The effect of titanium on the partitioning behavior of high-field strength elements between silicates, oxides and lunar basaltic melts with applications to the origin of mare basalts. *Chemical Geology* 440, 219–238.
- Leitzke, F.P., Fonseca, R.O.C., Sprung, P., Mallmann, G., Lagos, M., Michely, L.T., Münker, C. (2017) Redox dependent behaviour of molybdenum during magmatic processes in the terrestrial and lunar mantle: Implications for the Mo/W of the bulk silicate Moon. *Earth and Planetary Science Letters* 474, 503–515.
- Leitzke, F.P., Fonseca, R.O.C., Göttlicher, J., Steininger, R., Jahn, S., Prescher, C., Lagos, M. (2018) Ti K-edge XANES study on the coordination number and oxidation state of Titanium in pyroxene, olivine, armalcolite, ilmenite, and silicate glass during mare basalt petrogenesis. *Contributions to Mineralogy and Petrology* 173, 103.
- Lin, Y., Tronche, E.J., Steenstra, E.S., van Westrenen, W. (2017) Experimental constraints on the solidification of a nominally dry lunar magma ocean. *Earth and Planetary Science Letters* 471, 104–116.
- Longhi, J. (1992) Experimental petrology and petrogenesis of mare volcanics. *Geochimica et Cosmochimica Acta* 56, 2235–2251.
- Mallmann, G., O'Neill, H.St.C. (2009) The Crystal/Melt Partitioning of V during Mantle Melting as a Function of Oxygen Fugacity Compared with some other Elements (Al, P, Ca, Sc, Ti, Cr, Fe, Ga, Y, Zr and Nb). *Journal of Petrology* 50, 1765–1794.
- Mandl, M.B., Fehr, M.A., Schönbächler, M. (2018) Titanium stable isotope fractionation on the Moon: Evidence for inter-mineral isotopic fractionation. *Goldschmidt 2018* 2018, 1.
- Meyer, C. (2012) Lunar Sample Compendium. 10.
- Millet, M.-A., Dauphas, N. (2014) Ultra-precise titanium stable isotope measurements by double-spike high resolution MC-ICP-MS. *Journal of Analytical Atomic Spectrometry* 29, 1444.
- Millet, M.-A., Dauphas, N., Greber, N.D., Burton, K.W., Dale, C.W., Debret, B., Macpherson, C.G., Nowell, G.M., Williams, H.M. (2016) Titanium stable isotope investigation of magmatic processes on the Earth and Moon. *Earth and Planetary Science Letters* 449, 197–205.
- Münker, C. (2010) A high field strength element perspective on early lunar differentiation. *Geochimica et Cosmochimica Acta* 74, 7340–7361.
- Münker, C., Weyer, S., Scherer, E., Mezger, K. (2001) Separation of high field strength elements (Nb, Ta, Zr, Hf) and Lu from rock samples for MC-ICPMS measurements: SEPARATION OF HIGH FIELD STRENGTH ELEMENTS. *Geochemistry, Geophysics, Geosystems* 2, n/a-n/a.
- Poirasson, F., Halliday, A.N., Lee, D.-C., Levasseur, S., Teutsch, N. (2004) Iron isotope differences between Earth, Moon, Mars and Vesta as possible records of contrasted accretion mechanisms. *Earth and Planetary Science Letters* 223, 253–266.



- Poitrasson, F., Zambardi, T., Magna, T., Neal, C.R. (2019) A reassessment of the iron isotope composition of the Moon and its implications for the accretion and differentiation of terrestrial planets. *Geochimica et Cosmochimica Acta* 267, 257–274.
- Rapp, J.F., Draper, D.S. (2018) Fractional crystallization of the lunar magma ocean: Updating the dominant paradigm. *Meteoritics & Planetary Science* 53, 1432–1455.
- Ringwood, A.E. (1970) Special Papers-Apollo 11 Symposium: Petrogenesis of Apollo 11 Basalts and Implications for Lunar Origin. *Journal of Geophysical Research* 75, 6453–6479.
- Rudge, J.F., Reynolds, B.C., Bourdon, B. (2009) The double spike toolbox. *Chemical Geology* 265, 420–431.
- Schoenberg, R., Zink, S., Staubwasser, M., von Blanckenburg, F. (2008) The stable Cr isotope inventory of solid Earth reservoirs determined by double spike MC-ICP-MS. *Chemical Geology* 249, 294–306.
- Shaw, D.M. (1970) Trace element fractionation during anatexis. *Geochimica et Cosmochimica Acta* 34, 237–243.
- Shearer, C.K. (2006) Thermal and Magmatic Evolution of the Moon. *Reviews in Mineralogy and Geochemistry* 60, 365–518.
- Shih, C.-Y., Wiesmann, H.W., Haskin, L.A. (1975) On the Origin of High-Ti Mare Basalts. Sixth Lunar Science Conference 1975. Lunar and Planetary Institute, Houston, Abstract #1245.
- Snyder, G.A., Taylor, L.A., Neal, C.R. (1992) A chemical model for generating the sources of mare basalts: Combined equilibrium and fractional crystallization of the lunar magmasphere. *Geochimica et Cosmochimica Acta* 56, 3809–3823.
- Sossi, P.A., Moynier, F. (2017) Chemical and isotopic kinship of iron in the Earth and Moon deduced from the lunar Mg-Suite. *Earth and Planetary Science Letters* 471, 125–135.
- Sossi, P.A., O'Neill, H.St.C. (2017) The effect of bonding environment on iron isotope fractionation between minerals at high temperature. *Geochimica et Cosmochimica Acta* 196, 121–143.
- Sossi, P.A., Moynier, F., van Zuilen, K. (2018) Volatile loss following cooling and accretion of the Moon revealed by chromium isotopes. *Proceedings of the National Academy of Sciences* 115, 10920–10925.
- Sprung, P., Scherer, E.E., Upadhyay, D., Leya, I., Mezger, K. (2010) Non-nucleosynthetic heterogeneity in non-radiogenic stable Hf isotopes: Implications for early solar system chronology. *Earth and Planetary Science Letters* 295, 1–11.
- Sprung, P., Kleine, T., Scherer, E.E. (2013) Isotopic evidence for chondritic Lu/Hf and Sm/Nd of the Moon. *Earth and Planetary Science Letters* 380, 77–87.
- Thiemens, M.M., Sprung, P., Fonseca, R.O.C., Leitzke, F.P., Münker, C. (2019) Early Moon formation inferred from hafnium–tungsten systematics. *Nature Geoscience*.
- Trinquier, A., Elliott, T., Ulfbeck, D., Coath, C., Krot, A.N., Bizzarro, M. (2009) Origin of nucleosynthetic isotope heterogeneity in the solar protoplanetary disk. *Science* 324, 374–376.
- Tusch, J., Sprung, P., van de Löcht, J., Hoffmann, J.E., Boyd, A.J., Rosing, M.T., Münker, C. (2019) Uniform ^{182}W isotope compositions in Eoarchean rocks from the Isua region, SW Greenland: The role of early silicate differentiation and missing late veneer. *Geochimica et Cosmochimica Acta* 257, 284–310.
- van Kan Parker, M., Mason, P.R.D., van Westrenen, W. (2011) Trace element partitioning between ilmenite, armalcolite and anhydrous silicate melt: Implications for the formation of lunar high-Ti mare basalts. *Geochimica et Cosmochimica Acta* 75, 4179–4193.
- van Westrenen, W., Blundy, J.D., Wood, B.J. (2000) Effect of Fe²⁺ on garnet–melt trace element partitioning: experiments in FCMS and quantification of crystal-chemical controls in natural systems. 13.
- Walker, D., Longhi, J., Lasaga, A.C., Stolper, E.M., Grove, T.L., Hays, J.F. (1977) Slowly cooled microgabbros 15555 and 15065. *Lunar and Planetary Science Conference Proceedings* 2, 1521–1547.
- Wang, K., Jacobsen, S.B., Sedaghatpour, F., Chen, H., Korotev, R.L. (2015) The earliest Lunar Magma Ocean differentiation recorded in Fe isotopes. *Earth and Planetary Science Letters* 430, 202–208.
- Wang, W., Huang, S., Huang, F., Zhao, X., Wu, Z. (2019) Equilibrium inter-mineral titanium isotope fractionation: Implication for high-temperature titanium isotope geochemistry. *Geochimica et Cosmochimica Acta* S0016703719307069.
- Warren, P.H., Taylor, G.J. (2014) The Moon. *Treatise on Geochemistry*. Elsevier, 213–250.
- Warren, P.H., Wasson, J.T. (1979) The origin of KREEP. *Reviews of Geophysics* 17, 73.
- Weyer, S., Anbar, A., Brey, G., Munker, C., Mezger, K., Woodland, A. (2005) Iron isotope fractionation during planetary differentiation. *Earth and Planetary Science Letters* 240, 251–264.
- Zhang, J., Dauphas, N., Davis, A.M., Leya, I., Fedkin, A. (2012) The proto-Earth as a significant source of lunar material. *Nature Geoscience* 5, 251–255.

